A cloud-resolving simulation of Hurricane Bob (1991): Storm structure and eyewall buoyancy

Scott A. Braun

Laboratory for Atmospheres, NASA Goddard Space Flight Center,
Greenbelt, Maryland

April 12, 2001
Submitted to Monthly Weather Review

Corresponding author address: Dr. Scott A. Braun, Mesoscale Atmospheric Processes Branch, NASA GSFC, Code 912, Greenbelt, MD 20771.
E-mail: braun@agnes.gsfc.nasa.gov

ABSTRACT

A numerical simulation of Hurricane Bob (1991) is conducted using the Penn State University—National Center for Atmospheric Research mesoscale model MM5 with a horizontal grid spacing of 1.3 km on the finest nested mesh. The model produces a realistic hurricane that intensifies slowly during the period of fine-scale simulation. Time-averaged results reveal the effects of storm motion, vertical shear, beta gyres and deformation forcing on the structure of radial inflow, vertical motion, and precipitation. Instantaneous model fields show that radial inflow in the eyewall is very intense near the surface but transitions to strong low-level outflow near the top of the boundary layer. The low-level structure is modulated by a wavenumber 2 disturbance that rotates around the eyewall at half the speed of the maximum tangential winds and is consistent with a vortex Rossby edge wave. The statistical distribution of vertical velocity in the eyewall indicates that the eyewall is composed of a small number of intense updrafts that account for the majority of the upward mass flux rather than a more gradual and symmetric eyewall circulation, consistent with the concept of hot towers.

Tongues of high equivalent potential temperature, θ_e, are seen along the inner edge of the eyewall updraft and within the low-level outflow. This air originates from outside of the eyewall with the highest θ_e air coming from the layer closest to the surface after penetrating closest to the center. Occasionally, high θ_e air within the eye is drawn into the eyewall updrafts. The high θ_e air rising within the eyewall is shown to be associated with positive eyewall buoyancy with sufficient convective available potential energy along its path to produce relatively strong convective updrafts. Although the requirements for conditional symmetric instability are met within the eyewall and the air parcel trajectories follow slanted paths, the radial displacement of air parcels in the low-level outflow moves the air parcel sufficiently far away from the upper-level warm core that the air becomes unstable to vertical displacements. Hence, convective instability rather than symmetric instability accounts for the stronger updrafts in the eyewall.

A cloud-resolving simulation of Hurricane Bob (1991): Storm structure and eyewall buoyancy

Scott A. Braun

Summary

A computer simulation of a hurricane is conducted using a model with a horizontal grid spacing that is capable of resolving individual clouds. The model produces a realistic hurricane that intensifies slowly during the period of simulation. When averaged over time, the results reveal the effects of storm motion and vertical and horizontal variations in the environmental wind on the structure of inflow into the storm, rising motion in the wall of thunderstorms that surrounds the eye (known as the eyewall), and the associated precipitation. Instantaneous model fields show that inflow into the eyewall is very intense and shallow and transitions to strong outward flow just above the bases of the clouds in the eyewall. Statistical calculations indicate that the most of the upward motion in the hurricane eyewall is associated with a small number of intense but isolated thunderstorm updrafts instead of a broader region of more gentle upward motion, consistent with the concept of hot cloud towers.

Tongues of warm, moist air are seen along the inner edge of the eyewall updraft and within the low-level outward flow. This air originates primarily from outside of the eyewall and comes from the layer closest to the surface after penetrating closest to the storm center. The eye of the hurricane contains very warm air at upper levels that is generally believed to reduce or prevent the release of instabilities that produce thunderstorms. Some hypotheses suggest that the instability, rather than being released in the vertical direction, is instead released only along a slanted path outward and upward. This study shows that the low-level outward flow displaces the rising air sufficiently far away from the warm air in the eye so that the instability can be released in the vertical direction to produce thunderstorms rather than requiring that the air rise along a slanted path.

1. Introduction

Three-dimensional numerical simulations of tropical cyclones are being conducted at increasingly higher grid resolution, often reaching horizontal grid spacings of ~3-5 km (Tripoli 1992; Liu et al. 1997, 1999; Braun and Tao 2000). While use of this grid scale removes the necessity for parameterizing the effects of cumulus clouds, it may still not be fully adequate for resolving cloud-scale processes. This study presents a simulation of Hurricane Bob (1991) that uses a horizontal grid spacing of 1.3 km, which is typical of grid spacings used in most cloud-resolving models. The high spatial resolution provides an opportunity to examine the four-dimensional structure of a hurricane including a detailed investigation of the presence and magnitude of buoyancy in the eyewall.

Observations suggest that significant convective available potential energy (CAPE) exists in the outer regions of tropical cyclones, but decreases as one approaches the center as a result of decreasing surface temperatures and increasing upper-level temperatures associated with the warm core (Gray and Shea 1973; Bogner et al. 2000; Zhang et al. 2000). Gray and Shea (1973) remarked that assumption of a relative humidity of 100% in the eyewall leads to small vertical gradients of equivalent potential temperature (θ_e) and little diagnosed potential instability. However, they argued that only 10-20% of the eyewall may be occupied by active updrafts and that sinking motion between the updrafts and entrainment of dry air from the eye leads to a relative humidity that is often much less than 100%, which could support greater potential instability. Black et al. (1994) examined a hurricane with very strong vertical motions and suggested that significant CAPE could explain the intense updrafts. However, they also argued that the slantwise path of the rising air in the eyewall implicated moist symmetric instability as a possible mechanism. Under this instability, air that is stable to both vertical and horizontal displacements can be unstable with respect to slantwise displacements if the absolute angular momentum surfaces slope outward with height more than the θ_e surfaces.

Emanuel (1986) suggested that the hurricane eyewall is often close to a state of moist slantwise neutrality in which the θ_e and angular momentum surfaces are nearly parallel. This result implies that boundary layer air is neutrally buoyant when lifted along surfaces of constant angular momentum and that the vertical motions in the eyewall are largely determined by the magnitude of the vertical motions at the top of the boundary layer, i.e., little vertical acceleration occurs above the boundary layer. Tropical cyclones are envisioned to develop by self-induced anomalous fluxes of enthalpy from the sea surface with virtually no contribution from pre-existing CAPE in the surrounding environment (Rotunno and Emanuel 1987). Cumulus convection redistributes heat acquired from the sea surface in such a way as to maintain moist neutrality to slantwise motions. As Camp and Montgomery (2001) pointed out, Emanuel (1986) was not suggesting that hurricanes are entirely devoid of convective or slantwise instability, just that any buoyancy that develops is quickly eliminated. Camp and Montgomery further suggested that although the assumption of slantwise neutral conditions is not entirely correct, the Emanuel theory still captures a majority of the important dynamics.

This state of moist symmetric neutrality is most likely to be seen in mature tropical cyclones and in analyses of temporally and azimuthally averaged fields. Zhang et al. (2000) presented simulation results for Hurricane Andrew (1992) that indicated that the azimuthally averaged eyewall structure is characterized by potentially stable but slantwise unstable to neutral conditions. Examination of azimuthal averages, however, may mask the role of buoyant convection in the eyewall since active convection generally occupies only a small fraction of the eyewall (Riehl and Malkus 1961; Gray and Shea 1973). The scale of the convection is much smaller than that of the vortex and it is at these smaller scales that role of buoyancy must be examined. This study uses 2-min output from a 1.3-km grid-scale simulation of Hurricane Bob (1991) to examine the convective-scale structure of the buoyancy field and to calculate buoyancy along trajectories rising within the eyewall. The degree to which slantwise neutral conditions characterize the main regions of ascent within the eyewall is examined.

This study builds upon the simulations of Hurricane Bob by Braun and Tao (2000), who used a 4-km grid spacing to examine the sensitivity of the simulated hurricane to planetary boundary layer parameterizations. Here, the simulation is repeated for a shorter duration using a grid spacing of 1.3 km that is better able to resolve cloud microphysical processes. The paper is organized as follows. Section 2 summarizes the numerical model, the simulation methodology, analysis methods, and impacts of decreasing the grid spacing from 4 to 1.3 km. Section 3 describes characteristics of the time-averaged and instantaneous horizontal structure of kinematic and simulated radar reflectivity fields, and statistics related to updraft area and mass flux in the eyewall. Section 4 examines the thermodynamic structure of the storm including diagnostics of buoyancy in the eyewall. Finally, section 5 provides conclusions.

2. Simulation description

The model used in this study is the Pennsylvania State University—National Center for Atmospheric Research (PSU—NCAR) nonhydrostatic mesoscale model MM5 (V2.5; Dudhia 1993; Grell et al. 1995). A detailed description of the model setup is provided in Braun and Tao (2000) and is only briefly summarized here. The MM5 is used to conduct a 72-h simulation of Hurricane Bob (0000 UTC 16 August - 0000 UTC 19 August, 1991) using a coarse grid consisting of 193×163×27 grid points in x, y, and z on a Lambert conformal map projection with a grid spacing of 36 km. A high-resolution simulation is conducted by using 1-h output from the 36-km grid to provide initial and boundary conditions for a 12-km grid (163×178×27 grid points) beginning at hour 48 of the 72-h coarse-grid forecast. A 4-km grid is also initialized at 48 h by interpolating from the 12-km grid and, prior to 62 h, is moved with the storm in order to keep the storm nearly centered within the domain. Between 62-68 h, the 4-km grid is kept stationary and a 1.3-km grid is initialized and moved frequently to keep it centered on the storm.

Braun and Tao (2000) describe the model physics and derivation of initial and boundary conditions. Physics options for the 12-, 4-, and 1.3-km grids include the Betts-Miller cumulus

scheme on the 12-km grid, the Goddard Cumulus Ensemble Model (GCE) cloud microphysics scheme [modified as described in Braun and Tao (2000)], the Burk-Thompson boundary layer parameterization, and the Dudhia (1989) cloud radiation scheme. No cumulus parameterization is used on the 4- and 1.3-km grids.

The storm center is determined at every model output time using the pressure field at the lowest model level. Rather than using the location of the minimum pressure, which can lead to large oscillations of the eyewall about the center, the horizontal distribution of pressure is used to determine an approximate geometric center, or centroid, of the pressure field. This method leads to a more steady motion of the eyewall, but to oscillations of the surface low within the eye. The location of the minimum pressure is used as a first guess for the center. A variational approach is then used that adjusts the location of the center until the azimuthal variance of the pressure field at all radii between the center and the outer portion of the eyewall (~65 km) is minimized. This methodology works well not only at identifying the centroid of the pressure field, but also the approximate centroid of the ring of strong tangential winds and vorticity. The storm center location is kept constant with height, i.e., no attempt is made to determine different centers at higher levels. Storm motion is then computed from the identified center locations.

Because of the use of a Lambert conformal map projection, the horizontal wind components are not parallel to latitude and longitude lines. However, in the area of the hurricane, the angle between the model y-axis and longitude lines is only about 6.5°. Since this angle is relatively small, all analyses in this study use the winds parallel to the model axes. The wind component parallel to the y-axis is referred to as the "meridional" component while that parallel to the x-axis is the "zonal" component.

The environmental winds in the region of the storm are estimated by averaging the horizontal wind components over the region within 200 km of storm center using output from the 4-km grid. Because of the relatively small averaging area, the effects of beta gyres (Holland 1983; DeMaria 1985; Chan and Williams 1987; Fiorino and Elsberry 1989; Smith et al. 1990)

are included within this estimate of the environmental winds. The data are integrated vertically from p=900 to 150 hPa to determine estimates of the steering flow (Liu et al. 1999). Time series of the zonal and meridional components of the steering flow and storm motion are shown in Fig. 1a and indicate reasonable agreement. A hodograph of the storm-relative environmental flow is shown in Fig. 1b. The zonal component is weak below 12 km, but westerly flow up to 5 m s^{-1} occurs between 12-14 km associated with an approaching upper-level shortwave trough and easterly flow up to 2-4 m s^{-1} occurs above 15 km. The meridional component is characterized by northerly flow below 3 km and above 13 km and southerly flow in between peaking near 8 km.

Trajectories shown in later sections are calculated from the 2-min model output from the 1.3-km grid. A 10-s time step is used to calculate trajectory locations using wind fields interpolated linearly in time between model output times. Diagnostic fields such as winds, temperature, microphysical variables, and other fields are determined along the trajectories at 2-min intervals.

Fourier decomposition of the model fields is performed to separate the mean vortex (wavenumber 0) from higher wavenumber components. This analysis is accomplished by interpolating the model fields to a cylindrical grid with 1-km radial grid spacing and variable azimuthal spacing. Then, for each radius, the azimuthal variations are decomposed into different wavenumbers using fast fourier transform techniques.

Before examining the structure of the 1.3-km simulation in detail, it is instructive to compare it to the 4-km simulation described by Braun and Tao (2000). Important differences are seen that impact the intensity of the storm and its precipitation structure. The minimum central pressure of the storm, a measure of its intensity, is impacted by the decrease in grid spacing to 1.3 km. Figure 2 shows time series of the central pressure for the 6-h period of the 1.3-km simulation and the corresponding pressures from the 4-km simulation of Braun and Tao (2000) and observations. The 1.3-km simulation produces a weaker rate of intensification than that seen

in the 4-km simulation and observations with pressures in the latter 2.5 h being slightly above observed values and up to 4 hPa higher than the 4-km simulation.

The simulated precipitation structures indicate some key differences between the 1.3- and 4-km simulations. Figure 3 shows simulated radar reflectivities at 66 h for the 4-km simulation (Fig. 3a) and the 1.3-km simulation (Fig. 3b). In the 4-km simulation, the eyewall is the main precipitation feature, with only isolated convection or very light precipitation occurring outside of the eyewall. In the 1.3-km simulation (Fig. 3b), the rain distribution in the eyewall is generally similar to the 4-km simulation, but outside of the eyewall a prominent convective rainband is seen to the north and east of the eyewall. These results suggest that in the eyewall, where the forcing is strong, convection is easily produced on the 4-km grid even though the grid spacing is likely inadequate for resolving individual clouds, but that outside of the eyewall, where forcing is weaker, the 4-km grid is less able to initiate and maintain convection in this case.

3. Kinematic and reflectivity structure

a. Time-averaged structure

While instantaneous structures can provide insight into the evolution of the eyewall and rainbands, the tremendous temporal variability can mask the steadier structures. Before examining the instantaneous structure in the next subsection, the time-averaged fields are discussed. The time-averaged fields are obtained by compositing the 2-min model fields to a common grid using the center locations determined from section 2 and then averaging over the 6-h period of the 1.3-km simulation.

The 1.5-km level vertical velocity (Fig. 4) is typical of vertical motions at lower levels in this storm showing highly asymmetric structure with maximum values on the northwestern side of the storm. At upper levels (not shown), the strongest vertical motions tend to be found on the southeastern side of the storm because of the helical path of the updrafts. While rain at the surface surrounds the entire eye (Fig. 4a), it is maximum slightly downstream (in a cyclonic

sense) from the maximum vertical velocity as a result of cyclonic advection during fallout of the precipitating particles. The rain maximum is located to the left of the mean storm motion and wind shear vectors, while the vertical motion maximum is located in the left-front quadrant relative to the shear. This pattern is similar to that seen in modeling studies by Bender (1997) and Frank and Ritchie (1999). Jones (1995) and Frank and Ritchie (1999) have shown that for dry dynamics, tilting of the vortex by vertical shear produces a vertical velocity maximum in the downshear right quadrant, but simulations including moist convection by Bender (1997) and Frank and Ritchie (1999) shift the maximum to the downshear left side.

The near-surface tangential velocities (Fig. 4b) are maximum on the western side of the storm, just downstream from the vertical motion maximum with values exceeding 45 m s^{-1}. Near-surface radial inflow (Fig. 4c) surrounds the storm, with maximum inflow in the downshear left quadrant and weak outflow in the eye. The asymmetry of the inflow is partly related to the northeastward movement of the hurricane, which according to Shapiro (1983) should tend to produce strong inflow slightly to the right of the direction of storm motion. The location of strongest inflow to the left of the storm motion in this case is influenced by several factors that are apparent in the wavenumbers 1 and 2 components of the near-surface wind field (Fig. 5). The wavenumber 1 wind field is comprised of the effects of storm motion, vertical shear, beta gyres (Holland 1983; DeMaria 1985; Chan and Williams 1987; Fiorino and Elsberry 1989; Smith et al. 1990), as well as other asymmetries that can develop as a result of both internal dynamics (Peng and Williams 1990; Nolan and Montgomery 2000) and environmental forcing (Smith 1991; Kraus et al. 1995; Glatz and Smith 1996). Figure 5a shows that the wavenumber 1 flow is primarily from the north just outside the eye, which is more northerly than the flow direction associated with the storm-relative mean flow (Fig. 1b), although outside of a radius of 150 km (not shown) the flow direction is more consistent with the storm-relative flow. The influence of the beta gyres and other internal effects is diagnosed by removing the mean environmental flow from the wind field in Fig. 5a, the result of which is shown in Fig. 5b. The flow pattern

resembles the source-sink pattern described by Marks et al. (1992) in their analysis of Hurricane Norbert (1984), with convergence into the sink on the northern side of the eyewall and divergence out of the source on the southern side. The inflow is strongest on the northwestern side of the eyewall.

The wavenumber 2 pattern (Fig. 5c) shows inflow to the northwest and southeast of the eye and outflow to the northeast and southwest, which shifts the stronger inflow to the western side of the northern semicircle and to the eastern side of the southern semicircle. The flow is indicative of a deformation flow pattern that also extends out to much larger radii (>1000 km, not shown), suggesting that it is a product of the environmental flow. This environmental flow pattern is shown schematically in Fig. 6 and depicts southwesterly flow associated with an approaching trough to the west of the hurricane, southerly flow associated with the subtropical high to the east of the hurricane, and a weaker westerly flow to the southwest of the hurricane. When the storm motion is subtracted from this flow pattern, a clear deformation pattern is apparent with the axis of dilatation oriented southwest to northeast and the hurricane located at the center of the deformation pattern. To the extent that this pattern is typical of recurving storms prior to transition (Foley and Hanstrum 1994; Harr et al. 2000, Klein et al. 2000), deformation forcing may contribute to shifting the maximum inflow to the left of the storm motion in many transitioning storms. The fairly steady deformation forcing can also excite wavenumber 2 disturbances within the hurricane vortex (Kraus et al. 1995; Glatz and Smith 1996) that can influence the intensification of the storm (Montgomery and Kallenbach 1997).

b. Instantaneous low-level horizontal structure

The evolution of the reflectivity field at 1-km mean seal level (MSL) is shown in Fig. 7. The model produces an eyewall structure with precipitation that completely encloses the eye. This structure differs from that observed in Bob (Braun and Tao 2000), which had a partial eyewall structure throughout the majority of its lifetime. In this regard, the simulation is unable

to reproduce the observed structure and this error is likely due to initial condition errors, either in the initial vortex structure or the large-scale conditions. However, as will be shown, the simulation is very realistic in many ways and still provides insight into the structure of hurricanes in general.

Considerable fine-scale structure occurs within the eyewall (Fig. 7). At times (e.g., Figs. 7c, d), thin filaments of reflectivity are shed from the edge of the eyewall and may be associated with outward propagating inertia-gravity waves (Abdullah 1966; Senn and Hiser 1959; Willoughby 1977, 1978a, 1978b) or vortex Rossby waves (Guinn and Schubert 1993; Schubert et al. 1999). At 66 h (Fig. 7c), a well-developed convective rainband extends from the northwest side around to the east and south. Two hours earlier (Fig. 7a), the initial development of the convective rainband is apparent to the north and east of the eyewall. By 65 h (Fig. 7b), the convection moves outward somewhat and becomes more distinct from the eyewall, although weak reflectivities still occur between the rainband and the eyewall. By 66 h (Fig. 7c), this lighter precipitation diminishes and a precipitation-free zone extends toward the northwestern side of the storm. In the next hour (Fig. 7d), newly formed but weaker bands are produced along the eastern side of the storm and move into the region previously occupied by the convective rainband. These weaker bands are relatively short-lived, however. During the 6-h simulation, only a single long-lived, intense convective rainband forms outside of the eyewall, while the shorter-lived, weaker bands are nearly continually produced along the outer edges of the eyewall.

At 66 h, the tangential velocities at 500 m (Fig. 8) exceed 35 m s^{-1} within a 50- to 65-km wide band around the eye, with maximum winds generally ~65 m s^{-1} in isolated areas. While the tangential velocities decrease slowly with radius outside of the eyewall, the radial gradient of the tangential velocity on the inner side of the eyewall is very intense. The gradient is most intense on the western side and more relaxed on the eastern side of the eye, with vorticity values (not shown) reaching ~20×10^{-3} s^{-1}.

The horizontal structure of the radial velocity field at low levels within hurricanes has not been well documented since radar observations do not usually get below 500 m and the velocity field is often shown as an azimuthal average or vertical cross section. The simulation results are used here to characterize the near-surface radial velocities and the changes that occur rapidly while moving up through the boundary layer. Figure 9 shows the horizontal distribution of radial velocity at 100, 500, and 1500 m at 66 h. At 100 m (Fig. 9a), the radial velocity pattern shows strong inflow exceeding 15 m s^{-1} starting on the eastern side of the storm and extending around to the northern and western sides of the eyewall. Intense inflow greater than 30 m s^{-1} occurs on the northern side, just inside the maximum reflectivity of the eyewall, and on the western side within the high reflectivity area. Weaker inflow occurs on the southern side of the storm and also along the inner edge of the convective rainband to the northeast. Within the eye, weak outflow occurs and is strongest on the northwestern and southern sides of the eye. At 500 m (Fig. 9b), the inflow is weaker with a much smaller area of inflow exceeding 15 m s^{-1} on the northern and western sides of the eye. The weak inflow to the south outside of the eyewall at 100 m is transitioning to weak outflow at 500 m. Within the eye, the outflow has strengthened to 10-15 m s^{-1} within narrow bands on the inner edge of the eyewall. At 1500 m (Fig. 9c), the band of outflow around the eye is the primary feature with maximum outflow speeds of about 20-25 m s^{-1}. Weak inflow predominates on the northwestern side and weak outflow on the southeastern side outside of the eyewall.

The relationships between regions of maximum inflow and outflow and the wavenumber 2 wind and pressure perturbation fields are displayed in Fig. 10 for the lowest model level (42 m). The reflectivity field at this time (Fig. 7c) depicts an elliptically shaped eyewall with the major axis oriented west to east and stronger reflectivity regions at the ends of the major axis, similar to findings of Kuo et al. (1999). The wavenumber 2 pressure pattern shows areas of lower pressure at the ends of the major axis and higher pressure at the ends of the minor axis of the ellipse. The negative pressure perturbations are associated with cyclonic perturbation vorticity

while positive pressure perturbations are associated with anticyclonic vorticity (not shown). The perturbation wind fields therefore produce inflow ahead (in a cyclonic sense) of the lows and outflow ahead of the highs. The wavenumber 2 pattern is strongest in the radial band between 30-50 km, where the mean radial vorticity gradient is strongly negative. The wave pattern rotates around the center with constant angular velocity with a period of ~3.4 h or, assuming a radius of 40 km, at an average velocity of approximately 21 m s^{-1}, which is about half the mean azimuthal winds at this level. The slower phase speed of the asymmetry is consistent with the propagation of a wavenumber 2 vortex-Rossby edge wave (Kuo et al. 1999; Reasor et al. 2000). According to linear wave theory (Lamb 1932), the phase speed of a vortex-Rossby edge wave propagating on the vorticity discontinuity of a Rankine vortex is given by $c_p = V_m(1-1/n)$, where V_m is the maximum azimuthal-mean tangential wind and n is the azimuthal wavenumber. Therefore, for wavenumber 2, the phase speed is half the maximum tangential flow. However, other factors may also contribute to the excitation and maintenance of the wavenumber 2 pattern. For example, the potential vorticity (PV) distribution (not shown) is characterized by a ring of high PV near the radius of maximum wind, with lower PV in the center. This type of radial PV profile is barotropically exponentially unstable for wavenumber 2 (Reasor et al. 2000) and in the presence of sufficient PV production by convection in the eyewall, could maintain the wavenumber 2 asymmetry against the effects of vorticity mixing (Schubert et al. 1999). Also, persistent deformation forcing from the large-scale environment (Figs. 5c, 6) may favor development and maintenance of the wavenumber 2 asymmetry.

When the cyclonically propagating wavenumber 2 pattern is examined in combination with the wavenumbers 0 and 1 components of radial velocity (Fig. 5a), much of the transient structure of the radial velocity field can be understood. As a low pressure region associated with the wavenumber 2 asymmetry moves to the eastern side of the center, the inflow ahead of the low begins to overlap with the wavenumber 1 inflow region and produces a local maximum in inflow (Figs. 9a, 10). This pocket of strong inflow moves around to the northwestern side of the

storm with the low. As the low moves to the west of the center (Fig. 10, western low), the wavenumber 1 inflow transitions to outflow and nearly cancels the inflow ahead of the low to the southwest of the center. However, strong inflow still occurs on the western side of the storm as air converges into the low. The inflow associated with wavenumbers 0-2 ahead of the western low remains weak as the low subsequently moves around the southern side of the storm until the low again reaches the region of wavenumber 1 inflow in the northeastern quadrant. Ahead of the high pressure regions, the perturbation winds produce outflow from the eye or weaker inflow in the eyewall as can be seen in Fig. 10 to the northwest and southeast of the center.

c. Vertical structure

Vertical cross sections are shown in Figs. 11-13 and depict variations in the radial structure around the storm starting with a cross section to the northeast of the center and moving counterclockwise around the storm (see Fig. 7c). The cross section to the northeast cuts through the eyewall and convective rainband. Reflectivities (Fig. 11a) in the eyewall exceed 45 dBZ up to 5 km and upward vertical velocities (w) greater than 4 m s^{-1} occur just inside of the eyewall reflectivity maximum. Within the convective band, two cores of high reflectivity are present, the innermost one possessing reflectivities exceeding 45 dBZ up to 7-8 km. Both cores are associated with elevated updrafts with $w > 4$ m s^{-1}. Between the updrafts and extending below and just inside of the innermost core are downdrafts of 1-4 m s^{-1}.

To the northwest (Fig. 11b), the eyewall reflectivities and vertical velocities exhibit a greater outward slope with height. However, this slope is not the result of the tilt of a single updraft but is comprised of several updrafts that increase in depth with radius in a stair-step fashion. Vertical motions again are strongest inside the reflectivity maximum, reaching 4-6 m s^{-1}. At a radius of 125 km, a strong convective cell slopes inward with height with $w > 4$ m s^{-1} and reflectivities exceeding 45 dBZ up to 8 km. A strong upper-level downdraft occurs above and outside of this updraft. Between this cell and the eyewall, the precipitation is more stratiform-like

with embedded weak convection. The vertical motion field suggests a transition to stratiform structure between 75-115 km as the updraft broadens and rises and weak downward motion develops below.

Within the southwestern cross section (Fig. 11c), the reflectivities and vertical motions in the eyewall are somewhat weaker and the outward slope is even greater. Upward motions greater than 2 m s^{-1} extend up only to 4-5 km in the eyewall with downward motions at lower and upper levels along the inner edge of the eyewall. Outside of 50 km radius, the precipitation structure is definitely stratiform with weak upward motion above 5-7 km and weak downward motion below.

In the southeastern sector of the storm (Fig. 11d), the reflectivity structure is deep although the maximum reflectivities are weaker. The eyewall updraft and reflectivities are more upright with vertical motions of only 1-2 m s^{-1} inside the reflectivity maximum. In fact, in the deep reflectivity core between 50-75 km, the air motions are generally downward, suggesting that the precipitation has not been generated locally, but has been advected from the western side by the cyclonic flow. A very shallow and intense convective core occurs along the tail of the convective band (125 km) with the precipitation generated by warm microphysical processes only.

The radial velocities vary considerably around the storm. The primary outflow channel occurs in the upper troposphere in the southeastern and eastern sectors of the storm (Fig. 12d), with outflow exceeding 20 m s^{-1}, and tapers off toward the southwest and northeast. A secondary outflow layer occurs between 5-12 km MSL on the northern side of the storm (Figs. 12a, b) as a result of outflow from the convective rainband. In the northeastern cross section (Fig. 12a), outflow also occurs between the inner edge of the eyewall and the inner edge of the convective band between 3-7 km MSL. The northwestern cross section (Fig. 12b) cuts through the strong low-level outflow (Fig. 9c), with maximum outward flow along the inner edge of the eyewall reaching 25-30 m s^{-1} near 1-2 km. Similar, but weaker, outflow occurs in the southern cross

sections (Fig. 12c, d). The low-level outflow is similar to that seen in the analysis of Hurricane Allen (1980) by Jorgensen (1984) and in the simulation of Hurricane Andrew by Liu et al. (1997, 1999). Zhang et al. (2001) show that this outflow is associated with supergradient winds and suggest that it plays an important role in venting air from the eye.

The radial inflow is strongest on the northern side of the storm and decreases rapidly in strength with height. In the northern cross sections, inflow is briefly reduced across the convective band before increasing rapidly toward the center. In the southern cross sections, below 12 km, much deeper inflow occurs, particularly to the southeast, because of the south-southeasterly component of the storm-relative environmental flow (Fig. 1b).

d. Vertical mass flux statistics

Riehl and Malkus (1961) postulated that nearly all the mass reaching upper levels in the inner core ascends rapidly in a few nearly undilute convective hot towers rather than by a more uniform and gradual vertical mass circulation. Riehl and Malkus (1961) and Gray and Shea (1973) suggest that the percentage of the eyewall area occupied by these hot towers is relatively small, perhaps only 10-20%. In this section, the statistical distribution of vertical velocity within the eyewall is examined briefly to determine the contribution of hot towers to the total area and vertical mass flux within the eyewall. Histograms of vertical velocity are computed for all times and for each model level using a bin size of 0.5 m s^{-1} and enclosing the eyewall updrafts within a 25-km-wide radial band (Fig. 13). Results for the 5.2-km level are used as an example, but similar distributions exist at most levels between about 2-10 km MSL.

Figure 13 shows the instantaneous vertical velocity at 5.2 km MSL. Areas enclosed by the 2 m s^{-1} contours show that the updrafts are concentrated into cores that occupy only a small fraction of the eyewall area (i.e., the 25-km wide band) and typically enclose even more intense upward motions rather than comprising areas of somewhat broader-scale, gentle ascent. Figure 14a (dashed line) shows the cumulative percentage of the eyewall area with updrafts less than the indicated value using model output for the 6-h duration of the simulation. For example, updrafts

exceeding 2 m s^{-1} occupy only about 16% of the total eyewall area, while updrafts greater than 4 m s^{-1} occupy less than 7% of the eyewall area. The thick solid line in Fig. 14a shows the percentage of the *updraft area* occupied by updrafts with vertical motions less than the indicated value, with 30% (12%) of the updraft area being occupied by updrafts exceeding 2 m s^{-1} (4 m s^{-1}).

The percentage of the total upward mass flux coming from updrafts within 0.5 m s^{-1} bins centered on the indicated vertical velocities is shown in Fig. 14b (dashed line). The largest proportion of the upward mass flux at this level comes from vertical motions of about 1 m s^{-1}, a result consistent with those of Yuter and Houze (1995) for summertime convection in Florida, but peaking at somewhat smaller vertical velocities. However, the cumulative contribution to the total mass flux (thick solid line showing the percentage of the total upward mass flux coming from updrafts less than the indicated value) shows nearly 64% of the upward mass flux coming from updrafts stronger than 2 m s^{-1} and 37% coming from updrafts stronger than 4 m s^{-1}. Given the small area occupied by drafts greater than 2-4 m s^{-1} (Fig. 14a), this suggests that the hot towers account for a very large fraction of the total upward mass flux even though their total area is very small.

Even though the largest percentage of the upward mass flux comes from 1-2 m s^{-1} updrafts (dashed line in Fig. 14b), this does not necessarily mean that weaker stratiform-like updrafts between the updraft cores are contributing to the mass flux. Consider an isolated symmetric updraft core (Fig. 14c) that has peak intensity of ~10 m s^{-1} in its core and vertical velocities that fall off approximately as $1/r_c^2$, where r_c is the distance from the core center. In this regard, an updraft is viewed as having a distribution of vertical velocity within it as seen in Fig. 14d. For such an updraft, the area occupied by very intense vertical motions is small compared to that occupied by weaker drafts near its edge. The thin solid lines in Figs. 14a and 14b show the cumulative percentage of the updraft area and upward mass flux for this updraft and exhibit profiles very similar to that seen in the eyewall of the simulated hurricane. Therefore, the

contributions to the total upward mass flux from the weaker vertical motions may not generally be associated with stratiform precipitation processes but may merely represent the outer portions of updraft cores.

4. Thermodynamic structure

a. θ_e structure

An example of the thermodynamic structure is given in Fig. 15a, which shows a representative cross section of θ_e and radar reflectivity. High θ_e air is generally found in the boundary layer except where lower θ_e air has been brought into the boundary layer by downdrafts in the region of developing stratiform precipitation. Values of θ_e increase rapidly near the inner edge of the eyewall and a shallow pool of high θ_e air is found in the eye with θ_e reaching > 370 K. Above the boundary layer in the eye, θ_e decreases rapidly with height up to 2 km, remains relatively constant at ~350 K up to 7 km, and then increases gradually with height. This profile of θ_e is comparable to profiles derived from dropsondes in the eyes of hurricanes by Willoughby (1998).

A tongue of high θ_e air extends outward from the eye into the eyewall updraft and is nearly coincident with the low-level outflow above the boundary layer (Fig. 12b), giving the impression that the storm is drawing air out of the eye and into the updraft. Unlike the outer regions of the storm, where tongues of high θ_e air extend upward from the boundary layer in areas of convective updrafts (e.g., r=125 km), moist tongues in the eyewall are generally found along the inner edges of the updrafts (Fig. 15b). To examine how this structure occurs, trajectories are calculated for points initially located at the 2-km level that cut across both the updraft and high-θ_e tongue (Fig. 15b). The trajectories are started at 66 h and go backward 4 h and forward 2 h.

The trajectory paths are depicted in a radius-height cross section in Fig. 16a while the values of θ_e along portions of the trajectories are shown in Fig. 16b. Trajectories 1-3 originate

outside the eye, while trajectory 4 originates within the eye. Trajectory 1, which has the largest w but lowest θ_e of the trajectories at 2 km, descends from the 5-km level in the region of the convective band (not shown) and penetrates into the upper part of the boundary layer before rising within the eyewall. During its time in the boundary layer, the trajectory's θ_e increases 15 K from 337 to 352 K. Trajectory 2 starts near the 4-km level, descends to 1 km inside a radius of 100 km, and then penetrates lower down in the boundary layer, moving in closer to the center than trajectory 1. Its θ_e increases 19 K from 336 to 355 K before rising. Trajectory 3 lies below 0.6 km during the entire backward trajectory. It is closest to the surface and penetrates furthest into the eye, resulting in an increase of θ_e of 17 K from 340 to 357 K before rising. Trajectory 4 swirls around the eye, moving up and down nearly 1 km before getting caught up in the eyewall updraft and rising rapidly to upper levels. Its θ_e fluctuates ~5 K as it initially rises and falls within the eye and then decreases about 4 K as it rises within the eyewall, presumably because of mixing with drier air above the boundary layer in the eye (Fig. 15a). As trajectory 3 rises from near the surface, its θ_e continues to increase by about 2 K up to 1 km and then parallels that of trajectory 4 up to 2 km. Along trajectory 2, θ_e continues increasing up to 2 km before paralleling trajectory 4 up to 5 km. The θ_e profiles suggest that mixing occurs between some of the incoming air and the pool of high θ_e air in the eye.

Similar trajectories and θ_e profiles are seen along other sections of the storm, but do not always indicate air being drawn out of the eye by the low-level outflow, as in trajectory 4. Therefore, while low-level air within the eye is occasionally drawn into the updraft, the high θ_e air along the inner edge of the updraft and within the low-level outflow is predominantly associated with air that originates outside of the eyewall. This air generally comes from lower in the boundary layer and gets closer to the center so that it picks up more heat and moisture from the surface and reaches a lower pressure, thereby attaining the highest θ_e upon rising (Holland 1997; Liu et al. 1999). Some additional warming may be achieved through mixing with the low-level high θ_e air in the eye. Since air in the low-level outflow originates primarily from outside of

the eye, the eye is not being vented steadily by the outflow (Zhang et al. 2001), but more slowly by episodic "leakage" of eye air into the eyewall (Malkus 1958).

b. Buoyancy

Anecdotal evidence is first presented to demonstrate the characteristics of the vertical accelerations in the eyewall. Figure 17 shows profiles of vertical velocity and hydrometeor mixing ratios along trajectories 3 and 4 (Fig. 15b). For both trajectories, the vertical velocities increase with height from 0 near the surface to ~7-8 m s^{-1} near the melting level, demonstrating that the net effect of pressure and buoyancy forces at these levels is to accelerate the air upward. Trajectory 4 is more representative of many of the trajectories that have been calculated: rapid acceleration up to the freezing level followed by rapid deceleration, brief downward motion, and then recovery of weak upward motion aloft. The rapid deceleration above the freezing level generally coincides with the development of large graupel mixing ratios, with the transition to brief downward motion occurring immediately above the peak in graupel. This result suggests that hydrometeor water loading contributes significantly to decelerating the air parcels rising within the eyewall, in agreement with the findings of Zhang et al. (2000). As the graupel falls out of the parcels, water loading is reduced and weak upward accelerations recur. The parcels then rise more slowly (1-2 m s^{-1}) before reaching their equilibrium level near 14-15 km.

Zhang et al. (2000) used an MM5 simulation of Hurricane Andrew (1992) with 6-km grid spacing to investigate the vertical momentum budget and the role of buoyancy within the inner core of the storm. The azimuthally averaged eyewall was found to be potentially stable to vertical motions, but neutral or slightly potentially unstable to slantwise ascent. They concluded, however, that the vertical accelerations in the eyewall were attributable to small differences between positive (upward-directed) perturbation pressure gradient forces and negative (downward-directed) buoyancy and water loading forces, i.e., that air in the eyewall was negatively buoyant and was forced upward by perturbation pressure forces. An analysis of

buoyancy, however, is sensitive to the choice of a reference state. In Zhang et al. (2000), the reference state was obtained by performing a running average of the model output using four neighboring points on constant σ surfaces. This approach produces a reference state with considerable horizontal variability when applied to grid scales of less than 6 km. Also, their use of the pressure minimum as the center location instead of some measure of the geometric center may introduce some asymmetry in the eyewall.

This study advances an alternative definition of the reference state that uses fourier decomposition to divide the storm structure into its wavenumber 0 (azimuthal mean), wavenumber 1, and higher wavenumber contributions and includes the lower wavenumber fields in the reference state. This approach results in a horizontally smooth reference state and perturbations that cancel when averaged azimuthally. The motivation for this approach is as follows. First, the mass flux statistics from section 3d suggest that most of the ascent occurs within updrafts whose horizontal scale is much smaller than that of the mean vortex and wavenumber 1 asymmetry so that any buoyancy that exists would occur on similarly small scales. Second, the wavenumber 0 potential temperature field can be viewed as having little net impact on buoyancy since, for any given updraft parcel in the eyewall, adjacent air inside the parcel radius is warmer, adjacent air outside that radius is cooler, and adjacent air in the azimuthal direction has an identical temperature. Finally, the wavenumbers 0 and 1 potential temperature fields can be assumed to be approximately in thermal wind balance with the corresponding components of the tangential velocity. Departures from thermal wind balance on these scales, perhaps associated with frontogenesis in the eyewall (Emanuel 1997) or changes in the vertical shear associated with the vortex (Smith 1980), would likely produce weaker upward motion on the scale of the vortex rather than intense, small-scale updraft cores.

In general, positive buoyancy (in the absence of hydrometeor effects) is assumed to occur when the virtual potential temperature, θ_v, exceeds the local value associated with the broader-scale structure of the warm core. The virtual potential temperature excess can then be defined as

$\theta_v'(r,\lambda,z) = \theta_v(r,\lambda,z) - \theta_{v0}(z) - \theta_v^{0,1}(r,\lambda,z)$, where the prime denotes a perturbation value, the subscript 0 denotes a hydrostatic reference value, θ_{v0}, obtained by averaging over the 1.3-km model domain, and $\theta_v^{0,1}$ represents the perturbations associated with wavenumbers 0 and 1. Other perturbation variables can be defined analogously. The total buoyancy (Houze 1993) is defined as

$$B = g\left[\frac{\theta_v'}{\theta_{v0} + \theta_v^{0,1}} + (\kappa - 1)\frac{p'}{p_0 + p^{0,1}} - q_p'\right] \tag{1}$$

where κ=0.286, p is pressure, and q_p' is the perturbation hydrometeor mixing ratio (wavenumbers 2 and higher). Lower wavenumber components of q_p are not included in (1) since they contribute to hydrostatic balance between $\theta_v^{0,1}$ and $p^{0,1}$. Strictly speaking, the definition of buoyancy is based solely upon the perturbations from the reference state without regard to whether the air rises by purely vertical ascent or by slantwise ascent.

The virtual potential temperature excess, θ_v', overlaid on the vertical velocity field at the 3.2-km level is shown in Fig. 18. Areas of positive θ_v' (~0.5-3.5 K) are present in the eyewall, particularly on the western and eastern sides of the storm where updrafts are strongest and low-level pressure perturbations are negative (Fig. 10). Cross sections through the convection on the northwestern side of the storm in Fig. 19 depict the vertical structure of the reference state ($p^{0,1}$ and $\theta_v^{0,1}$, with horizontal means p_0 and θ_{v0} excluded), the higher wavenumber perturbations p' and θ_v', and the buoyancy defined in (1). The reference pressure field (Fig. 19a) shows a strong low pressure perturbation at low levels in the eye and relatively higher pressures outside the eyewall. The vertical pressure gradient force is directed downward in the eye and eyewall and upward outside of the eyewall and is in hydrostatic balance with the warm temperature anomaly

in the eye[1] (Fig. 19b) and the low wavenumber hydrometeor fields $q_p^{0,1}$ (not shown). Closer in scale to the convection, the higher wavenumber perturbation pressures (Fig. 19c) indicate negative values (~3-4 hPa) underneath and just inside of the deep convection, maximum near the surface and decreasing with height. The vertical gradients of both the reference state and perturbation pressures are thus directed downward in the eyewall and, in contrast to Zhang et al. (2000), do not appear to contribute to lifting of the low-level air. Areas of low-level positive p' (Fig. 10) have upward directed perturbation pressure gradient forces, but tend to be characterized by weaker updrafts or weak downdrafts at mid levels. The θ_v' values (Fig. 19d) are maximum in the eyewall convection and reach values of up to 4 K. The effects of hydrometeor drag act to reduce the buoyancy (Fig. 19e) associated with θ_v', but still indicate positive buoyancy in the eyewall up to near 5 km with only weak buoyancy above.

The patterns shown in individual cross sections of the storm (Fig. 19) are not necessarily representative of rising air parcels, however, since the rising air moves a significant distance azimuthally around the storm during the time that it ascends from the lower to upper troposphere. In order to examine the vertical accelerations of air rising in the eyewall, the perturbation temperature θ_v', buoyancy, and vertical pressure gradient force have been calculated along trajectory 3 (Fig. 17a) by subtracting the time-dependent reference values following the trajectory (Fig. 20). Between 1-11 km, θ_v' is 1-2 K resulting in buoyancy that is generally positive except below 1 km and above 9.5 km. The vertical pressure gradient force largely opposes the buoyancy force. The negative buoyancy below 1.5 km means that the air is initially lifted out of the boundary layer by perturbation pressure forces, in relative agreement with Zhang et al. (2000). However, above this level, the perturbation pressure gradient force is directed

[1] In this depiction of the warm anomaly, the core of the anomaly is located much lower than is typically observed (e.g., Hawkins and Imbembo 1976) because of the removal of a domain averaged value, which contains some signature of the inner-core warming. When a reference profile characteristic of the large-scale environment outside of the storm is subtracted from the inner-core potential temperatures, the core of the warm anomaly is located close to 9-10 km, in better agreement with observations within hurricanes.

downward so that upward accelerations are the result of the positive buoyancy. The vertical velocity tendency, $\Delta w/\Delta t$, estimated from the 2-min output along the trajectory, and the vertical force balance [$B+(1/\rho)\partial p'/\partial z$, where ρ is the air density] along the trajectory (Fig. 20b) show good agreement below 8 km and *confirm the important role of positive buoyancy and not upward directed pressure forces in accelerating the upward motion in the eyewall above the boundary layer*. The poor agreement between the two profiles in Fig. 20b between 8.5 and 10.5 km may be the result of two factors: 1) the coarser vertical resolution at these levels, which may cause increased errors in the calculation of the vertical pressure gradient; and 2) the fact that $\Delta w/\Delta t$ is determined over 2-min intervals while the vertical force balance is an instantaneous value.

The negative buoyancy and upward-directed pressure force at low levels are related to the wavenumber 2 structure of the eyewall (Fig. 10). The wavenumber 2 pattern rotates around the storm at about half the speed of the tangential flow so that low-level inflowing air moves through the pattern. During the time that the buoyancy is negative and the pressure gradient force is directed upward, the air parcel associated with trajectory 3 is moving through the wavenumber 2 positive pressure perturbation on the north side of the eyewall (Fig. 10). As the parcel rises above the boundary layer, it moves through the wavenumber 2 pattern from the high pressure region to the low pressure region and becomes positively buoyant while the pressure gradient force changes to a downward direction to oppose the buoyancy. The wavenumber 2 disturbance thus modulates the upward motion and precipitation development within the eyewall through its impact on the buoyancy and pressure forces at low levels.

The average buoyancy along the trajectory below 12 km is approximately 80 m s^{-1} h^{-1}, yielding a CAPE of ~445 J kg^{-1} when water loading effects are excluded and ~260 J kg^{-1} when they are included. These values of CAPE are more than adequate for generating updrafts of up to 10 m s^{-1} if one assumes that the maximum vertical velocity is given by $w_{max}=(2\cdot \mathrm{CAPE})^{1/2}$ (Weisman and Klemp 1986).

The buoyancy is generally achieved along outward slanted paths along which absolute angular momentum ($M = rV + fr^2/2$, r =radius, f=Coriolis parameter) is nearly conserved, although along some trajectories substantial variations in M can occur. Emanuel (1986) and Rotunno and Emanuel (1987) have suggested that the mature hurricane eyewall is characterized by a state of moist symmetric neutrality in which the saturated equivalent potential temperature, θ_{es}, and M surfaces are parallel. Zhang et al. (2000), in their simulation of Hurricane Andrew, found that the azimuthal mean eyewall was near neutral or characterized by slight potential symmetric instability (θ_e and M surfaces nearly parallel). Figure 21a shows the azimuthal mean distributions of M and θ_{es} for Hurricane Bob. Within the eyewall between 2-5 km MSL, the θ_{es} contours are nearly vertical while the M contours slope outward, so that $\partial\theta_{es}/\partial z<0$ along the M surfaces and the requirement for conditional symmetric instability is met. These results then motivate the question, are the updrafts the result of symmetric instability?

A hypothetical air parcel rising out of the boundary layer along the thick solid line in Fig. 21a starts with a relatively high value of θ_e that remains nearly constant during ascent (Fig. 21b; here, trajectory 3 is used to depict the parcel θ_e and environmental θ_{es}). If the azimuthally averaged fields approximately represent the environment into which the parcel rises, then the environmental θ_{es} decreases with height up to about 3 km and then increases above that height (dashed line in Fig. 21b). The parcel θ_e exceeds θ_{es} of the environment up to a height of 10.5 km. As a result, relatively large slantwise CAPE, or SCAPE, exists within the eyewall. Interestingly, after the air parcel is "flung" outward by the low-level outflow (r~40 km, z~1.5 km in Fig. 21a), its θ_e is sufficiently high that it could, in the absence of horizontal forces, rise vertically to the upper troposphere without any further outward displacement, i.e., it is unstable to vertical displacements. Of course, as shown by Zhang et al. (2001), supergradient forces arising from upward angular momentum transport accelerate the rising air outward so that it continues along a slantwise path. Recall that symmetric instability occurs only when an air parcel is *stable* to purely vertical and horizontal displacements and *unstable* to slantwise displacements.

Consequently, after the initial outward displacement at low levels, the attribution of strong ascent to symmetric instability is not justified since the air is *unstable* to further vertical displacements.

These results have implications for the development within hurricanes of convective bursts (Steranka et al. 1986; Heymsfield et al. 2001), which are episodes of prolonged deep convection in or near the eyewall. Outside of the eyewall, sufficient CAPE may exist to support deep convection, but within the eyewall the warm anomaly is often thought to eliminate any CAPE required for deep convection. However, when the low-level outflow in the eyewall is strong, the radial displacement can be adequate to allow for deep convection to develop even in a mature hurricane.

The findings of significant buoyancy within the updraft cores and the fact that most of the eyewall vertical mass flux is associated with small-scale updrafts that occupy only a fraction of the eyewall area support the notion of the eyewall containing active "hot towers" (Riehl and Malkus 1958; Simpson et al. 1998). An important question is, what is the dynamical role of the hot towers? Are they just aberrations on the mean (symmetric) dynamics or are they the essential components of the dynamics? The results of this study suggest that the concept of a symmetrically rising current of air within the eyewall, while convenient for theoretical purposes, is rather unrepresentative of actual processes in the eyewall since much of the eyewall upward mass flux is occurring within isolated hot towers. However, it may be that development of the mean vortex depends only on the amount of air rising within the eyewall rather than on how the air rises. Since the upward motion is concentrated into small cores, the immediate impacts of the convection (e.g., potential vorticity changes) must also occur on small scales but then feedback to the mean vortex rapidly through axisymmetrization processes because of the preferential decay of high wavenumber asymmetries (Smith and Montgomery 1995). A future study will examine the role of vortex Rossby waves and axisymmetrization using this simulation.

5. Conclusions

A simulation of Hurricane Bob (1991) is conducted using a grid spacing (1.3 km) typical of many convective cloud models. While the simulation does not reproduce the highly asymmetric precipitation structure of Bob, it realistically produces many features of observed hurricanes.

The time-averaged structure is characterized by maximum low-level vertical motions and inflow in the left-front quadrant relative to the storm motion and mean wind shear vectors and maximum precipitation and tangential winds located to the left of these vectors. While the storm motion is expected to produce maximum inflow in the right-front quadrant (Shapiro 1983), the maximum inflow is shifted to the left-front quadrant by the effects of wavenumber 1 asymmetries associated with internal dynamics as well as by wavenumber 2 asymmetries associated with deformation forcing. The deformation forcing is associated with a large-scale environment in which the hurricane is located between an approaching short-wave trough to the west and the subtropical high to the east, a pattern that is fairly typical of recurving storms.

The simulation produces a realistic eyewall and a single well-defined, long-lived convective rainband that slowly moves outward from the eyewall. Other shorter-lived and weaker rainbands are frequently shed from the eyewall and may be associated with outward propagating gravity waves or vortex Rossby waves. Radial inflow is very intense near the surface, but weakens rapidly through the boundary layer, transitioning to intense low-level outflow near the top of the boundary layer within some portions of the eyewall. The low-level structure is strongly modulated by a pronounced wavenumber 2 disturbance that creates an elliptically shaped eyewall. The disturbance rotates around the eye at about half the speed of the maximum tangential winds, consistent with theory for vortex Rossby edge waves. Other potential source mechanisms for this wavenumber 2 disturbance include counter-propagating

vortex Rossby waves that form in the region of a barotropically unstable mean radial vorticity gradient and the large-scale deformation forcing.

Examination of the radial distribution of θ_e reveals that in the eyewall, tongues of high θ_e air extend upward from the boundary layer in the eye along the inner edge of the eyewall updrafts instead of being collocated with the updrafts, as is seen in convection outside of the eyewall. Trajectory calculations suggest that the air in these high θ_e tongues generally originates from outside of the eyewall, with the highest θ_e air coming from very near the surface, where it picks up substantial heat and moisture, and penetrating furthest into the eye before rising, allowing the parcels to reach lower pressures and possibly mix with high θ_e air in the eye boundary layer. Occasionally, high θ_e air within the eye is drawn into the eyewall updrafts.

Calculated eyewall trajectories possess strong vertical accelerations up to the melting level, above which water loading significantly dampens the accelerations or reverses them until precipitation falls out. To explain the vertical accelerations, buoyancy is diagnosed by decomposing the thermodynamic fields into different azimuthal wavenumber components and including wavenumbers 0 and 1 in the reference state. Results show considerable buoyancy in the eyewall with virtual potential temperature perturbations up to 4 K. Buoyancy calculated along a trajectory for an air parcel rising within the eyewall shows sufficient CAPE to account for the simulated vertical velocities. Unlike the study of Zhang et al. (2000), which suggested that dynamic pressure perturbations forced negatively buoyant eyewall air to rise through the depth of the troposphere, the results here suggest that such pressure forces act only to lift the air out of the boundary layer, after which positive buoyancy is responsible for the upward accelerations.

The buoyancy in the eyewall is concentrated into small-scale regions of upward motion in the eyewall. The statistical distribution of vertical velocity within the eyewall indicates that the majority of the upward mass flux occurs within small cores of more intense vertical motions rather than in a broader ring of more gentle upward motion. These results reaffirm the

importance of convective "hot towers" as the main mechanism for vertical transport of mass in the eyewall.

The buoyancy is most often achieved along outward sloping paths rather than along purely vertical paths. Comparison of azimuthal mean fields of absolute angular momentum and saturated equivalent potential temperature reveal a layer below the melting level in which the requirements for conditional symmetric instability are met, thereby suggesting that symmetric instability is responsible for the buoyancy and accelerations. However, as boundary layer air rises, it is ejected outward by the low-level supergradient outflow. After just 1-2 km of ascent above the surface, the air has moved sufficiently far away from the upper-level warm core that it is unstable to vertical displacements through much of the rest of the troposphere even if no further outward displacements occur. Thus, the small-scale, intense updrafts are generally a product of convective instability rather than symmetric instability. This finding implies that idealized models of hurricanes (Emanuel 1986, 1999) that assume that the eyewall is composed of more gradual ascent associated with symmetrically neutral conditions may be assuming an unrealistic representation of the buoyancy and vertical motions within the eyewall. Further research is required to assess the impact of assumptions about the character of the vertical circulation in the eyewall (buoyant, localized updrafts versus symmetrically neutral, broader-scale ascent) on theories and modeling of the intensification process.

This study has focused on the basic kinematic and thermodynamic structures of the simulated hurricane using a model grid resolution that is adequate for resolving cloud-scale processes. The high frequency of output (2 min) allows for detailed examination of the evolution of both vortex-scale and convective-scale features of the storm structure. Research is in progress that focuses on the evolution of vortex Rossby waves, their relationship to convective processes in the eyewall, and their role in vortex intensification through eddy momentum and heat transports. Toward this goal, calculations of momentum and heat budgets will be presented in future studies.

Acknowledgements: The author gratefully acknowledges Michael Montgomery, Joanne Simpson, John Fulton, and Jeffery Halverson for their many helpful comments and discussions. Mark Stoelinga provided the software used for generating several of the figures as well as for calculating the trajectories. Acknowledgement is also made to Dr. R. Kakar (NASA/HQ) for his support of this research and NASA Goddard Space Flight Center for computer time used in the research.

REFERENCES

Abdullah, A. J., 1966: The spiral bands of a hurricane: A possible dynamic explanation. *J. Atmos. Sci.*, **23**, 367-375.

Bender, M. A., 1997: The effect of relative flow on the asymmetric structure in the interior of hurricanes. *J. Atmos. Sci.*, **54**, 703-724.

Black, R. A., H. B. Bluestein, and M. L. Black, 1994: Unusually strong vertical motions in a Caribbean hurricane. *Mon. Wea. Rev.*, **122**, 2722-2739.

Bogner, P. B., G. M. Barnes, and J. L. Franklin, 2000: Conditional instability and shear for six hurricanes over the Atlantic Ocean. *Wea. Forecasting*, **15**, 192-207.

Braun, S. A., and W.-K. Tao, 2000: Sensitivity of high-resolution simulations of Hurricane Bob (1991) to planetary boundary layer parameterizations. *Mon. Wea. Rev.*, **128**, 3941-3961.

Camp, J. P., and M. T. Montgomery, 2001: Hurricane maximum intensity: Past and present. *Mon. Wea. Rev.*, (in press).

Chan, J. C., and R. T. Williams, 1987: Analytic and numerical studies of the beta-effect in tropical cyclone motion. Part I: Zero mean flow. *J. Atmos. Sci.*, **44**, 1257-1265.

DeMaria, M., 1985: Tropical cyclone motion in a nondivergent barotropic model. *Mon. Wea. Rev.*, **113**, 1199-1210.

Dudhia, J., 1993: A nonhydrostatic version of the Penn State-NCAR mesoscale model: Validation tests and simulation of an Atlantic Cyclone and cold front. *Mon. Wea. Rev.*, 121, 1493-1513.

Emanuel, K. A., 1986: An air-sea interaction theory for tropical cyclones. Part I.: Steady-state maintenance. *J. Atmos. Sci.*, **43**, 585-604.

———, 1997: Some aspects of hurricane inner-core dynamics and energetics. *J. Atmos. Sci.*, **54**, 1014-1026.

———, 1999: Thermodynamic control of hurricane intensity. *Nature*, **401**, 665-669.

Fiorino, M., and R. L. Elsberry, 1989: Some aspects of vortex structure related to tropical cyclone motion. *J. Atmos. Sci.*, **46**, 975-990.

Foley, G. R., and B. N. Hanstrum, 1994: The capture of tropical cyclones by cold fronts off the west coast of Australia. *Wea. Forecasting*, **9**, 577-592.

Frank, W. M., and E. A. Ritchie, 1999: Effects of environmental flow upon tropical cyclone structure. *Mon. Wea. Rev.*, **12**, 2044-2061.

Glatz, A., and R. K. Smith, 1996: Vorticity asymmetries in Hurricane Josephine (1984). *Quart. J. Roy. Meteor. Soc.*, **122**, 391-413.

Gray, W. M., and D. J. Shea, 1973: The hurricane inner core region. II. Thermal stability and dynamic characteristics. *J. Atmos. Sci.*, **30**, 1565-1576.

Grell, G. A., J. Dudhia, and D. R. Stauffer, 1995: A description of the fifth-generation Penn State/NCAR Mesoscale Model (MM5). NCAR Technical Note (NCAR/TN-398+STR), 122 pp.

Guinn, T. A., and W. H. Schubert, 1993: Hurricane spiral bands. *J. Atmos. Sci.*, **50**, 3380-3403.

Harr, P. A., and R. L. Elsberry, 2000: Extratropical transition of tropical cyclones over the western North Pacific. Part I. Evolution of structural characteristics during the transition process. *Mon. Wea. Rev.*, **128**, 2613-2633.

Heymsfield, G. M., J. Halverson, J. Simpson, L. Tian, and T. P. Bui, 2001: ER-2 Doppler radar (EDOP) investigations of the eyewall of Hurricane Bonnie during CAMEX-3. *J. Appl. Meteor.*, (submitted).

Holland, G. J., 1983: Tropical cyclone motion: Environmental interaction plus a beta effect. *J. Atmos. Sci.*, **40**, 328-342.

———, 1997: The maximum potential intensity of tropical cyclones. *J. Atmos. Sci.*, **54**, 2519-2541.

Houze, R. A. Jr., 1993: *Cloud Dynamics*, Academic Press, 573 pp.

Jones, S. C., 1995: The evolution of vortices in vertical shear: Initially barotropic vortices. *Quart. J. Roy. Meteor. Soc.*, **121**, 821-851.

Jorgensen, D. P., 1984: Mesoscale and convective-scale characteristics of mature hurricanes. Part II: Inner core structure of Hurricane Allen (1980). *J. Atmos. Sci.*, **41**, 1287-1311.

Klein, P. M., P. A. Harr, and R. L. Elsberry, 2000: Extratropical transition of western North Pacific tropical cyclones: An overview and conceptual model of the transformation stage. *Wea. Forecasting*, **15**, 373-395.

Kraus, A. B., R. K. Smith, and W. Ulrich, 1995: The barotropic dynamics of tropical cyclone motion in a large-scale deformation field. *Contrib. to Atmos. Phys.*, **68**, 249-261.

Kuo, H.-C., R. T. Williams, and J.-H. Chen, 1999: A possible mechanism for the eye rotation of Typhoon Herb. *J. Atmos. Sci.*, **56**, 1659-1673.

Lamb, H. 1932: *Hydrodynamics*. 6th ed. Dover, 732 pp.

Liu, Y., D.-L. Zhang, and M. K. Yau, 1997: A multiscale numerical study of Hurricane Andrew (1992). Part I: Explicit simulation and verification. *Mon. Wea. Rev.*, **125**, 3073-3093.

Liu, Y., D.-L. Zhang, and M. K. Yau, 1999: A multiscale numerical study of Hurricane Andrew (1992). Part II: Kinematics and inner-core structures. *Mon. Wea. Rev.*, **127**, 2597-2616.

MacDonald, N. J., 1968: The evidence for the existence of Rossby-like waves in the hurricane vortex. *Tellus*, **20**, 138-150.

Malkus, J. S., 1958: On the structure and maintenance of the mature hurricane eye. *J. Meteor.*, **15**, 337-349.

Marks, F. D., R. A. Houze, Jr., and J. F. Gamache, 1992: Dual-aircraft investigation of the inner core of Hurricane Norbert. Part I: Kinematic structure. *J. Atmos. Sci.*, **49**, 919-942.

Montgomery, M. T., and R. J. Kalenbach, 1997: A theory for vortex Rossby waves and its application to spiral bands and intensity changes in hurricanes. *Quart. J. Roy. Meteor. Soc.*, **123**, 435-465.

Nolan, D. S., and M. T. Montgomery, 2000: The algebraic growth of wavenumber one disturbances in hurricane-like vortices. *J. Atmos. Sci.*, **57**, 3514-3538.

Reasor, P. D., M. T. Montgomery, F. D. Marks, and J. F. Gamache, 2000: Low-wavenumber structure and evolution of the hurricane inner core observed by airborne dual-Doppler radar. *Mon. Wea. Rev.*, **128**, 1653-1680.

Riehl, H., and J. S. Malkus, 1961: Some aspects of Hurricane Daisy, 1958. *Tellus*, **13**, 181-213.

Rotunno, R., and K. A. Emanuel, 1987: An air-sea interaction theory for tropical cyclones. Part II: Evolutionary study using a nonhydrostatic axisymmetric numerical model. *J. Atmos. Sci.*, **44**, 542-561.

Senn, H. V., and H. Hiser, 1959: On the origin of hurricane spiral rainbands. *J. Meteor.*, **16**, 419-426.

Shapiro, L. J., 1983: The asymmetric boundary layer flow under a translating hurricane. *J. Atmos. Sci.*, **40**, 1984-1998.

Smith, G. B., and M. T. Montgomery, 1995: Vortex axisymmetrization: Dependence on azimuthal wavenumber or asymmetric radial structure changes. *Quart. J. Roy. Meteor. Soc.*, **121**, 1615-1650.

Smith, R. K., 1991: An analytic theory of tropical cyclone motion in a barotropic shear flow. *Quart. J. Roy. Meteor. Soc.*, **117**, 685-714.

———, W. Ulrich, and G. Dietachmayer, 1990: A numerical study of tropical cyclone motion using a barotropic model. Part I: The role of vortex asymmetries. *Quart. J. Roy. Meteor. Soc.*, **116**, 337-362.

Steranka, J., E. B. Rogers, and R. C. Gentry, 1986: The relationship between satellite measured convective bursts and tropical cyclone intensification. *Mon. Wea. Rev.*, **114**, 1539-1546.

Tripoli, G. J., 1992: An explicit three-dimensional nonhydrostatic numerical simulation of a tropical cyclone. *Meteorol. Atmos. Phys.*, **49**, 229-254.

Weisman, M. L., and J. B. Klemp, 1986: Characteristics of isolated convective storms. *Mesoscale Meteorology and Forecasting*, (Ed. P. S. Ray), American Meteorological Society, Boston, 793 pp.

Willoughby, H. E., 1977: Inertia-buoyancy waves in hurricanes. *J. Atmos. Sci.*, **34**, 1028-1039.

———, 1978a: A possible mechanism for the formation of hurricane rainbands. *J. Atmos. Sci.*, **35**, 838-848.

———, 1978b: The vertical structure of hurricane rainbands and their interaction with the mean vortex. *J. Atmos. Sci.*, **35**, 849-858.

———, 1979: Excitation of spiral bands in hurricanes by interaction between the symmetric mean vortex and a shearing environmental steering current. *J. Atmos. Sci.*, **36**, 1226-1235.

———, 1998: Tropical cyclone eye thermodynamics. *Mon. Wea. Rev.*, **126**, 3053-3067.

Yuter, S. E., and R. A. Houze, Jr., 1995: Three-dimensional kinematic and microphysical evolution of Florida cumulonimbus. Part III: Vertical mass transport, mass divergence, and synthesis. *Mon. Wea. Rev.*, **123**, 1964-1983.

Zhang, D.-L., Y. Liu, and M. K. Yau, 2000: A multiscale numerical study of Hurricane Andrew (1992). Part III: Dynamically induced vertical motion. *Mon. Wea. Rev.*, **128**, 3772-3788.

———, ———, ———, 2001: A multiscale numerical study of Hurricane Andrew (1992). Part IV: Unbalanced flows. *Mon. Wea. Rev.*, **129**, 92-107.

FIGURE CAPTIONS

Figure 1. (a) Time series of the meridional (thick lines) and zonal (thin lines) components of the storm motion (U_S, V_S, dashed lines) and the vertically integrated environmental steering flow ($\{U_E\}$, $\{V_E\}$, solid lines), where the brackets { } indicate a vertical average. (b) Hodograph of the storm-relative environmental flow. Diamonds indicate values at the given model height level (km).

Figure 2. Time series of minimum sea-level pressure from observations (thick solid line), the 4-km simulation (thin solid line), and the 1.3-km simulation (dashed line).

Figure 3. Simulated radar reflectivity patterns at 1 km MSL at 66 h (valid at 1800 UTC 18 August 1991) for (a) the 4-km simulation and (b) the 1.3-km simulation. Panel (a) shows only a subset of the 4-km domain while panel (b) shows the entire 1.3-km domain. Tick marks are drawn every 8 km with large tick marks every 40 km.

Figure 4. Time averaged (a) rain mixing ration, (b) tangential velocity, and (c) radial velocity at the lowest model level (42 m). Shading indicates 1.5-km level vertical velocity with contours drawn at 1 and 2 m s^{-1} (light and dark shading, respectively). In (a), contours are drawn at intervals of 0.5 g kg^{-1}, starting at 0.5 g kg^{-1}. The dark arrow indicates the storm motion, the light arrow the direction of the surface to 8-km wind shear vector. In (b), contours are drawn at 5 m s^{-1} intervals, with the 35 m s^{-1} contour highlighted by a dashed line. In (c), contours are drawn at 5 m s^{-1} intervals. Unless mentioned otherwise, positive (negative) values are indicated by solid (dashed lines) in all figures.

Figure 5. Isotachs of radial velocity and total wind vectors at the lowest model level (42 m) for (a) the wavenumber 1 component of the storm-relative flow; (b) as in (a), but with the mean environmental flow removed; and (c) the wavenumber 2 component of the flow. Shading indicates the band of wavenumber 0 inflow greater than 20 m s^{-1}. In (a) and (b), the contour interval is 2 m s^{-1}. In (c), contours are drawn at ±0.5, 1.5, and 2.5 m s^{-1}. The vector scale is shown in the upper-right corner of each panel. The bold arrow in the lower-right corner of (a) indicates the direction of the 42-m level storm-relative flow (Fig. 1b).

Figure 6. Schematic diagram illustrating the synoptic flow pattern in the environment of Hurricane Bob. Dark lines indicate the ground-relative flow while lighter lines indicate the storm-relative flow. Thicker (thinner) lines indicates stronger (weaker) flow. The circle represents the hurricane and the small arrow indicates the direction of its movement. The letters "H" and "L" indicate regions of higher and lower synoptic-scale pressure.

Figure 7. Simulated radar reflectivity patterns at 1 km MSL at (a) 64 h, (b) 65 h, (c), 66 h, and (d) 67 h. Tick marks are drawn every 8 km with large tick marks every 40 km. Solid lines in (c) show the locations of radial cross sections.

Figure 8. Tangential velocity at 500 m at 66 h. The contour interval is 5 m s^{-1}. Tick marks are drawn every 8 km with large tick marks every 40 km.

Figure 9. Radial velocity at 66 h at (a) 100 m, (b) 500 m, and (c) 1500 m. The contour interval is 5 m s^{-1}. Tick marks are drawn every 8 km with large tick marks every 40 km.

Figure 10. Wavenumber 2 pressure perturbation and wind vectors superimposed on the radial velocities (shading). The pressure perturbation is contoured at ±0.5 and 1.5 hPa. The vector scale is shown above the upper-left corner.

Figure 11. Vertical velocity (thin contours and shading) and radar reflectivity (bold contours) for radial cross sections starting at storm center and extending to the (a) northeast, (b) northwest, (c) southwest, and (d) southeast of the storm. Cross section locations are indicated in Fig. 7c. Vertical velocity contours are drawn at ±0, 1, 2, 4, 6, and 8 m s^{-1}. Reflectivity contours are drawn at 15, 30, and 45 dBZ.

Figure 12. As in Fig. 11, but for radial velocity, contour interval of 5 m s^{-1}, with light (dark) shading indicating outflow greater than 5 m s^{-1} (10 m s^{-1}).

Figure 13. Horizontal distribution of vertical velocity at 5.2 km MSL and 66 h. The contour interval is 2 m s^{-1} with the zero contour excluded. Rings at 35 and 60 km radius indicate the annular region used to compute statistics in the eyewall.

Figure 14. (a) Curves show the cumulative percentage of the area occupied by all updrafts less than the magnitude given on the abscissa. The dashed line shows the percentage of the total eyewall area while the thick solid line shows the percentage of the total updraft area in the eyewall (i.e., excludes the areas occupied by downdrafts). The thin solid line is similar to the thicker line, but corresponds to the hypothetical updraft in panels (c) and (d). (b) The dashed line shows the percentage of the upward mass flux associated with updrafts falling within 0.5 m s^{-1} bins centered on the indicated values of vertical velocity. The thick solid line indicates the cumulative percentage of the upward mass flux coming from updrafts less than the indicated value. The thin solid line corresponds to the hypothetical updraft. (c) The horizontal distribution

of vertical velocity associated with a hypothetical circular updraft core. Contours are drawn at 2 m s^{-1} intervals with an additional contour at 1 m s^{-1}. (d) The radial distribution of vertical velocity associated with the hypothetical updraft, where the radius refers to the distance from the updraft center.

Figure 15. (a) Vertical cross section of θ_e (thin lines, shading) and radar reflectivity (bold contours) for the northwest cross section (cf. Fig. 7c). The contour interval for θ_e is 5 K, with light (dark) shading indicating values greater than 345 K (355 K). Reflectivity contours are drawn at 15, 30, and 45 dBZ. (b) θ_e (contours) and vertical velocity (shading) for a subset of the region in (a). Light (dark) shading corresponds to vertical velocities greater than 1 m s^{-1} (4 m s^{-1}). Trajectory locations are indicated by the dots with the numbers 1-4 identifying the trajectories.

Figure 16. (a) Profiles of trajectory radius versus height for the trajectories with initial positions indicated in Fig. 15b. Only radii less than 100 km are shown. (b) Trajectory θ_e versus height. Only θ_e values greater than 350 K are shown.

Figure 17. Profiles of vertical velocity (solid lines) and total hydrometeor mixing ratio (q_p, dashed line) versus height for (a) trajectory 3 and (b) trajectory 4.

Figure 18. Horizontal cross section of vertical velocity (light shading > 1 m s^{-1}, dark shading > 3 m s^{-1}) and perturbation virtual potential temperature (positive contours only, drawn at 1 K intervals starting at 0.5 K) associated with wavenumbers 2 and higher at the 3.2 km level at 66 h. The line indicates the location of the vertical cross sections in Fig. 19.

Figure 19. Vertical cross sections of (a) $p^{0.1}$ (2 hPa contour interval), (b) $\theta_v^{0.1}$ (2 K interval), (c) p' (wavenumbers 2 and higher, 0.5 hPa interval), (d) θ_v' (1 K intervals starting at 0.5 K), and (e)

buoyancy B (100 m s^{-1} h^{-1} intervals starting at 100 m s^{-1} h^{-1}). In (d, e), only positive values are contoured for clarity.

Figure 20. (a) Vertical profiles of w (thick solid line), θ_v' (thin solid line),B (dashed line), and the vertical perturbation pressure gradient force (dotted line) following trajectory 3. (b) Profiles of the vertical velocity tendency (solid line) and the vertical force balance (dashed line).

Figure 21. (a) Radial cross section of the azimuthal mean θ_{es} (solid lines, 2 K intervals) and M (dashed lines, 0.25×10^6 s^{-1} intervals). The light shading indicates the area of the azimuthal mean eyewall updraft while the thick solid line depicts a hypothetical air parcel trajectory in the radius-height plane. (b) Profiles of environmental θ_{es} (dashed line) and air parcel θ_e (solid line) following an air parcel rising in the eyewall [obtained from trajectory 3, but intended here to illustrate profiles along the bold line in (a)].

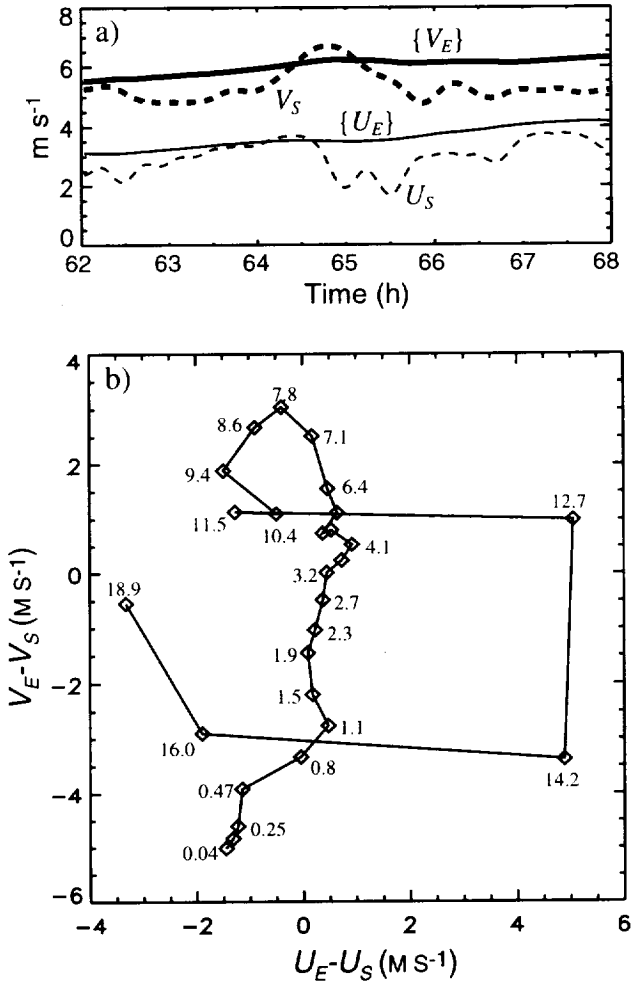

Figure 1. (a) Time series of the meridional (thick lines) and zonal (thin lines) components of the storm motion (U_S, V_S, dashed lines) and vertically integrated environmental steering flow ($\{U_E\}$, $\{V_E\}$, solid lines), where the brackets { } indicate a vertical average. (b) Hodograph of the storm-relative environmental flow. Diamonds indicate values at the given model height level (km).

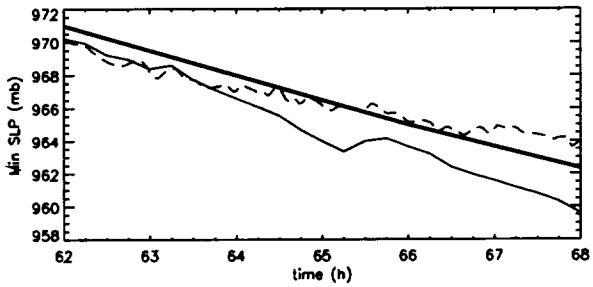

Figure 2. Time series of minimum sea-level pressure from observations (thick solid line), the 4-km simulation (thin solid line), and the 1.3-km simulation (dashed line).

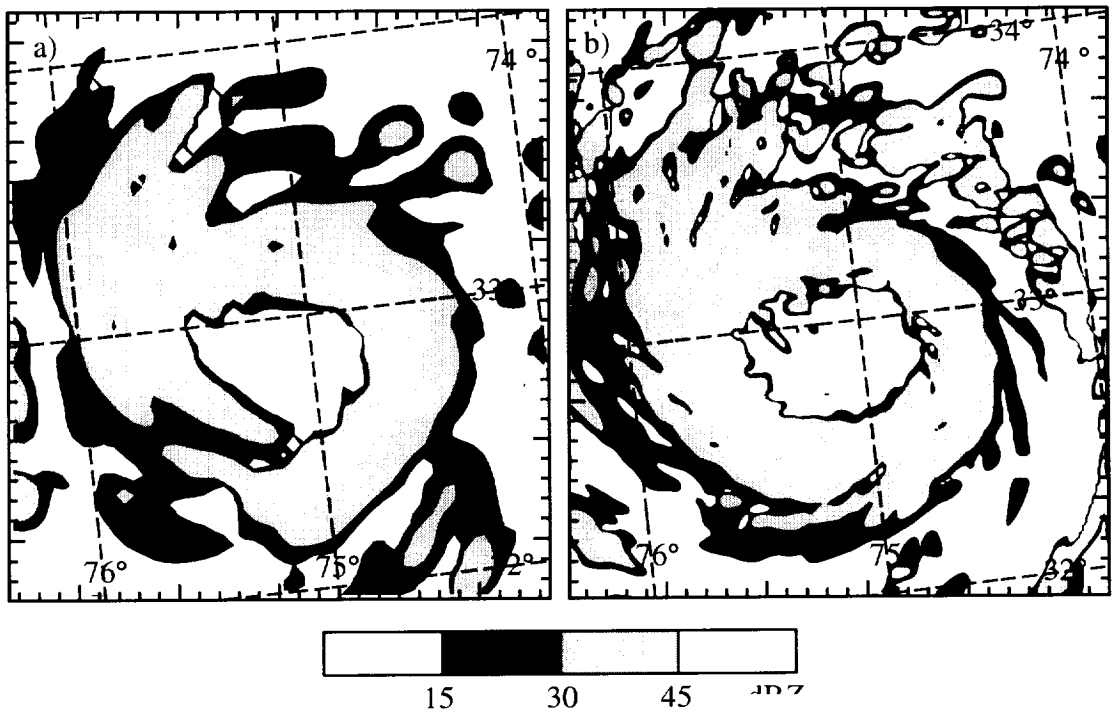

Figure 3. Simulated radar reflectivity patterns at 1 km MSL at 66 h (valid at 1800 UTC 18 August 1991) for (a) the 4-km simulation and (b) the 1.3-km simulation. Panel (a) shows only a subset of the 4-km domain while panel (b) shows the entire 1.3-km domain. Tick marks are drawn every 8 km with large tick marks every 40 km.

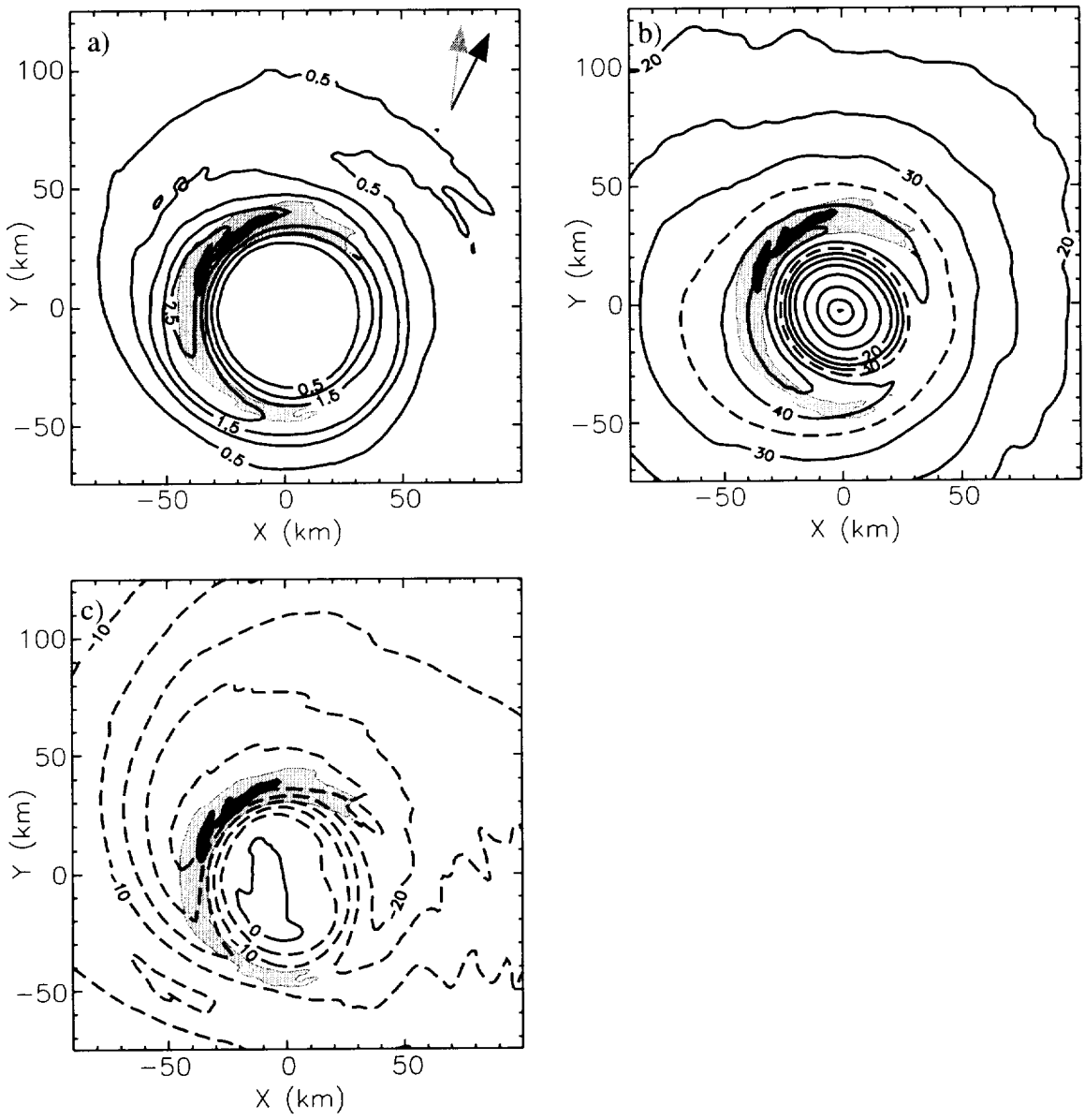

Figure 4. Time averaged (a) rain mixing ratio, (b) tangential velocity, and (c) radial velocity at the lowest model level (42 m). Shading indicates 1.5-km level vertical velocity with contours drawn at 1 and 2 m s^{-1} (light and dark shading, respectively). In (a), contours are drawn at intervals of 0.5 g kg^{-1}, starting at 0.5 g kg^{-1}. The dark arrow indicates the storm motion, the light arrow the direction of the surface to 8-km wind shear vector. In (b), contours are drawn at 5 m s^{-1} intervals, with the 35 m s^{-1} contour highlighted by a dashed line. In (c), contours are drawn at 5 m s^{-1} intervals. Unless mentioned otherwise, positive (negative) values are indicated by solid (dashed) lines in all figures.

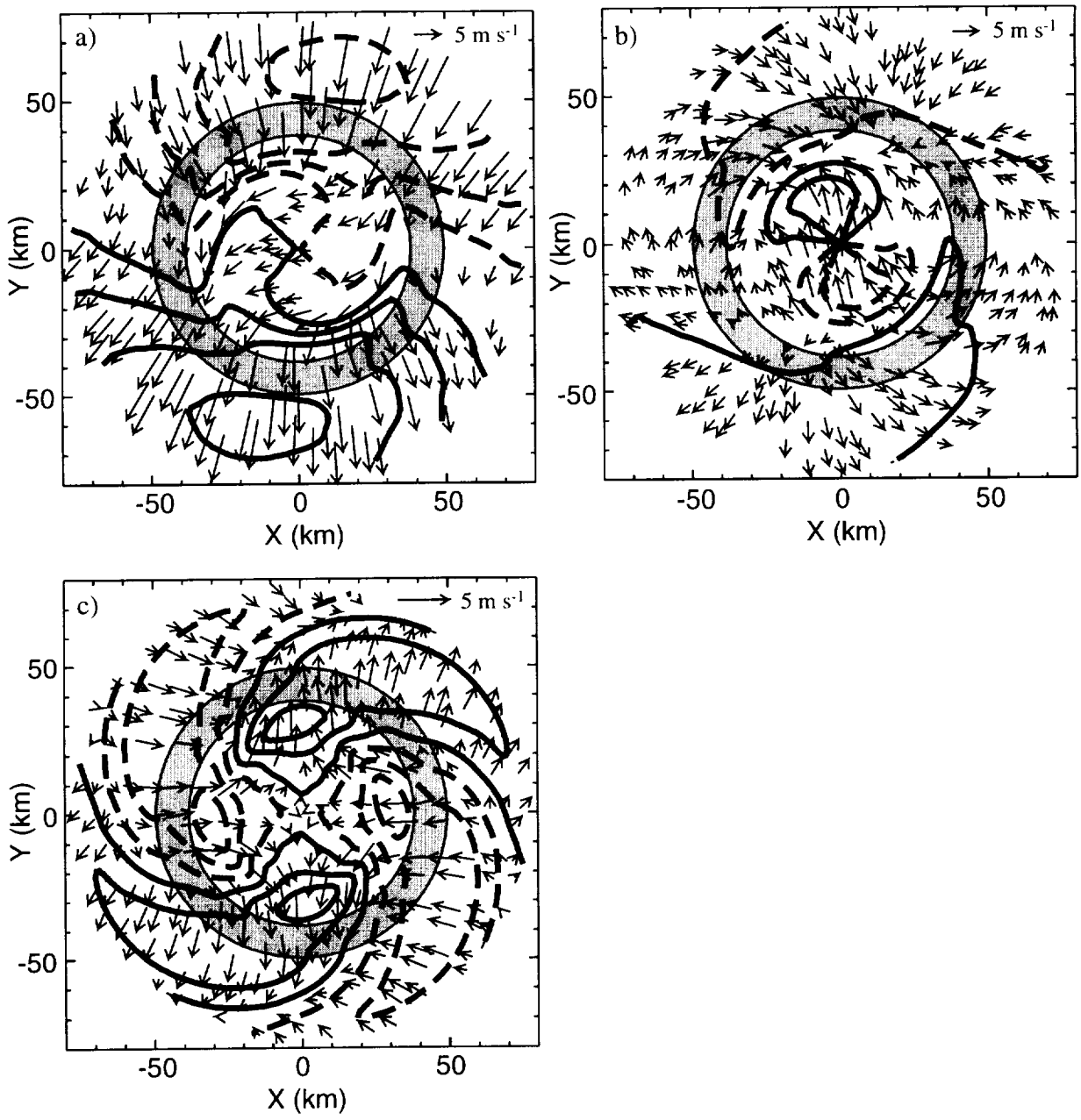

Figure 5. Isotachs of radial velocity and total wind vectors at the lowest model level (42 m) for (a) the wavenumber 1 component of the storm-relative flow; (b) as in (a), but with the mean environmental flow removed; and (c) the wavenumber 2 component of the flow. Shading indicates the band of wavenumber 0 inflow greater than 20 m s^{-1}. In (a) and (b), the contour interval is 2 m s^{-1}. In (c), contours are drawn at +/– 0.5, 1.5, and 2.5 m s^{-1}. The vector scale is shown in the upper right corner of each panel. The bold arrow in the lower-right corner of (a) indicates the direction of 42-m level storm-relative flow (Fig. 1b).

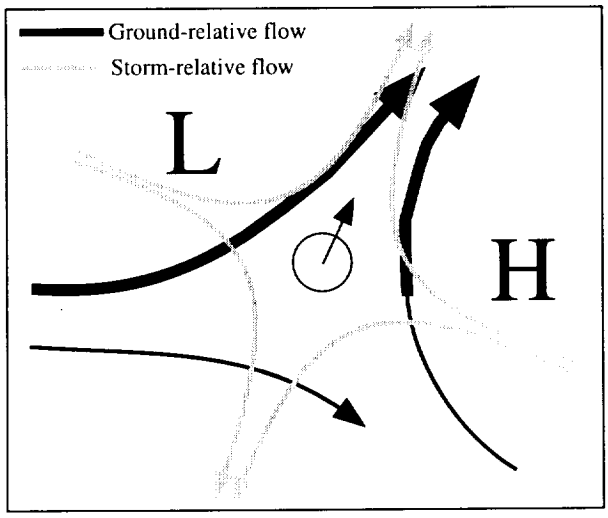

Figure 6. Schematic diagram illustrating the synoptic flow pattern in the environment of Hurricane Bob. Dark lines indicate the ground-relative flow while lighter lines indicate the storm-relative flow. Thicker (thinner) lines indicate stronger (weaker) flow. The circle represents the hurricane and the small arrow indicates the direction of its movement. The letters "H" and "L" indicate regions of higher and lower synoptic scale pressure.

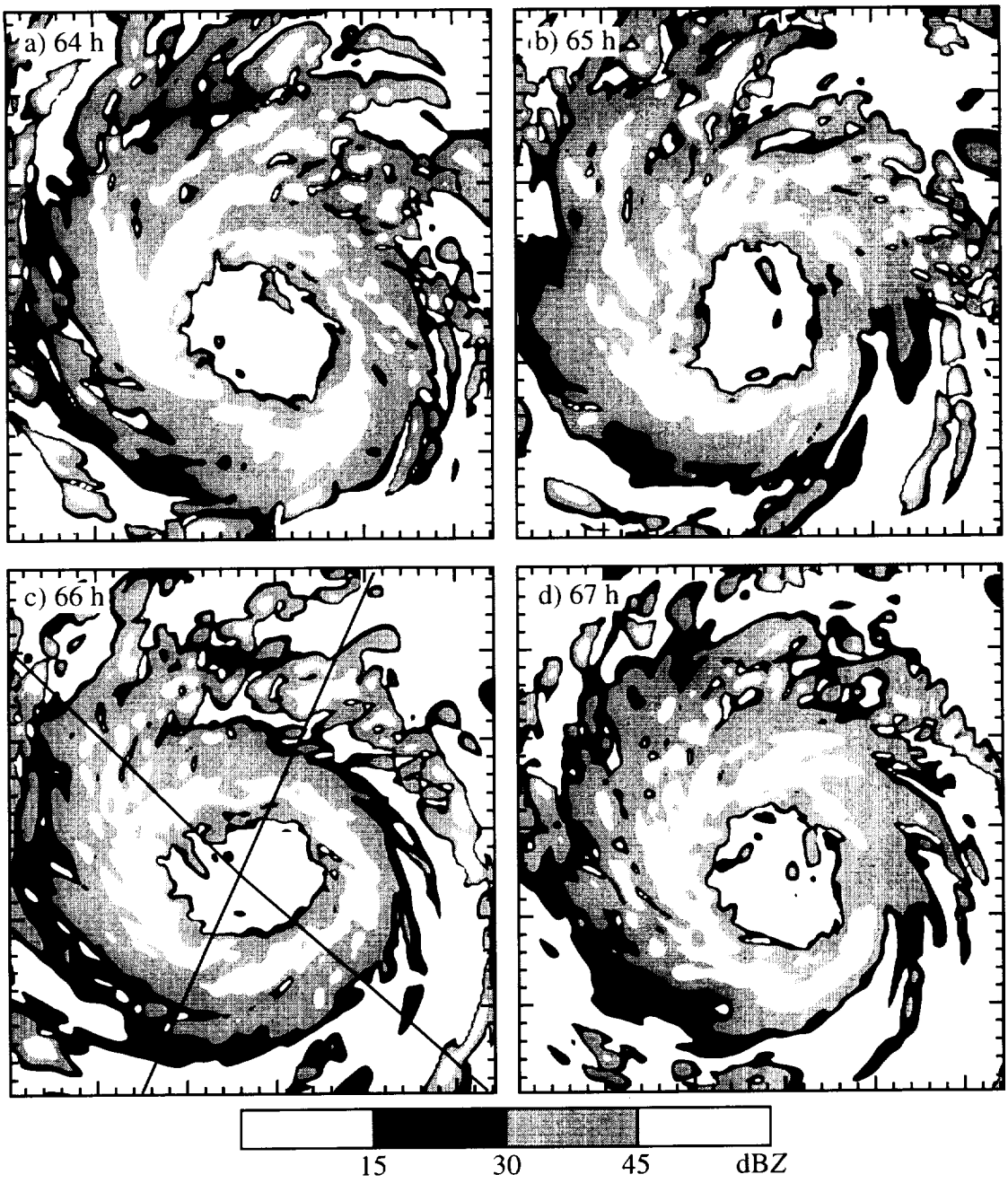

Figure 7. Simulated radar reflectivity patterns at 1 km MSL at (a) 64 h, (b) 65 h, (c) 66 h, and (d) 67 h. Tick marks are drawn every 8 km with large tick marks every 40 km. Solid lines in (c) show the locations of radial cross sections.

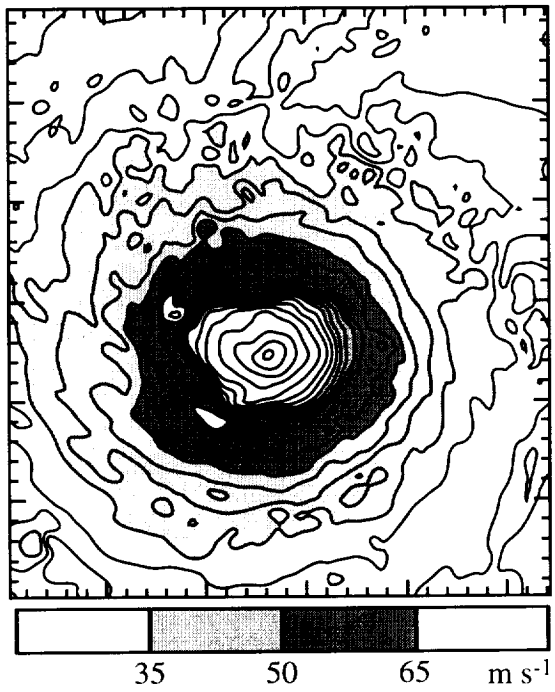

Figure 8. Tangential velocity at 500 m at 66 h. The contour interval is 5 m s^{-1}. Tick marks are drawn every 8 km with large tick marks every 40 km.

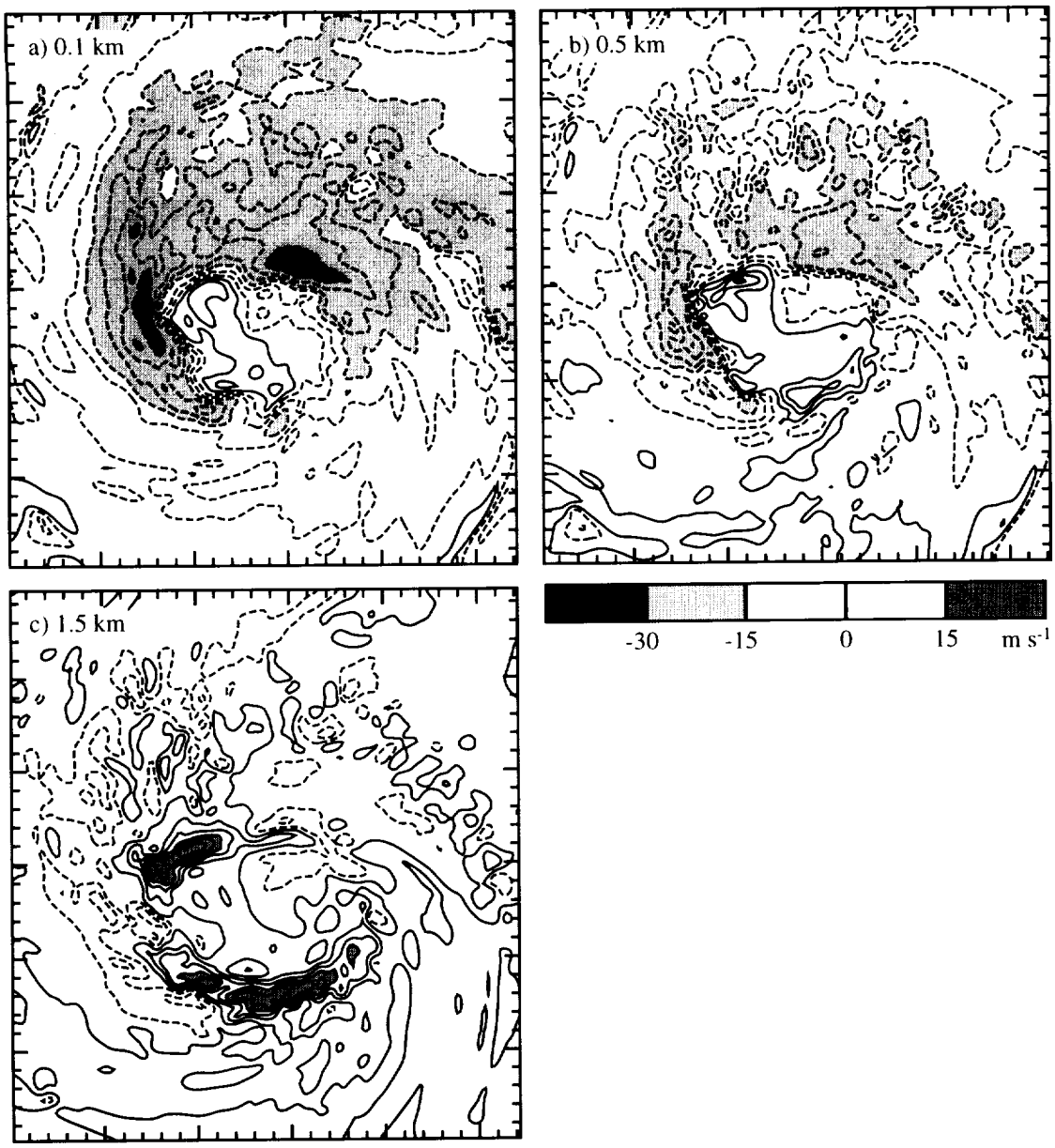

Figure 9. Radial velocity at 66 h at (a) 100 m, (b) 500 m, and (c) 1500 m. The contour interval is 5 m s^{-1}. Tick marks are drawn every 8 km with large tick marks every 40 km.

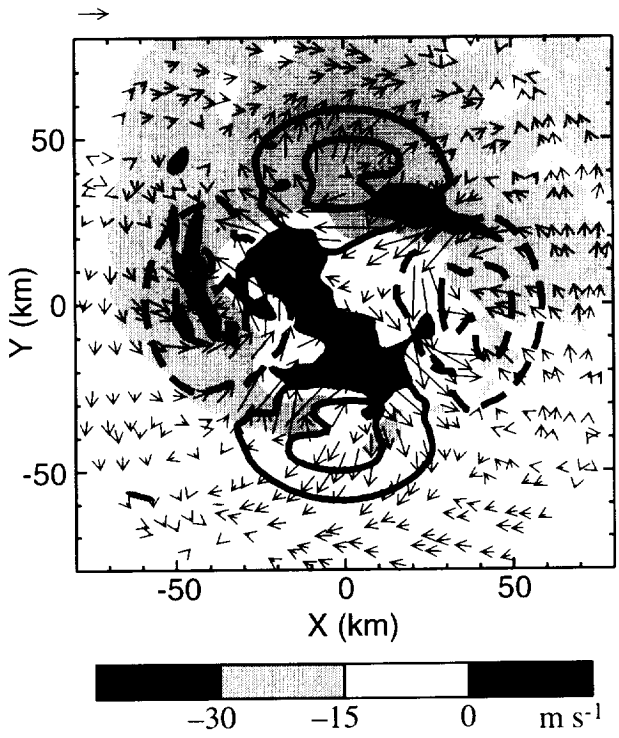

Figure 10. Wavenumber 2 pressure perturbation and wind vectors superimposed on the radial velocities (shading) at 125 m MSL. The pressure perturbation is contoured at +/–0.5 and 1.5 mb. The vector scale is shown in the upper left corner.

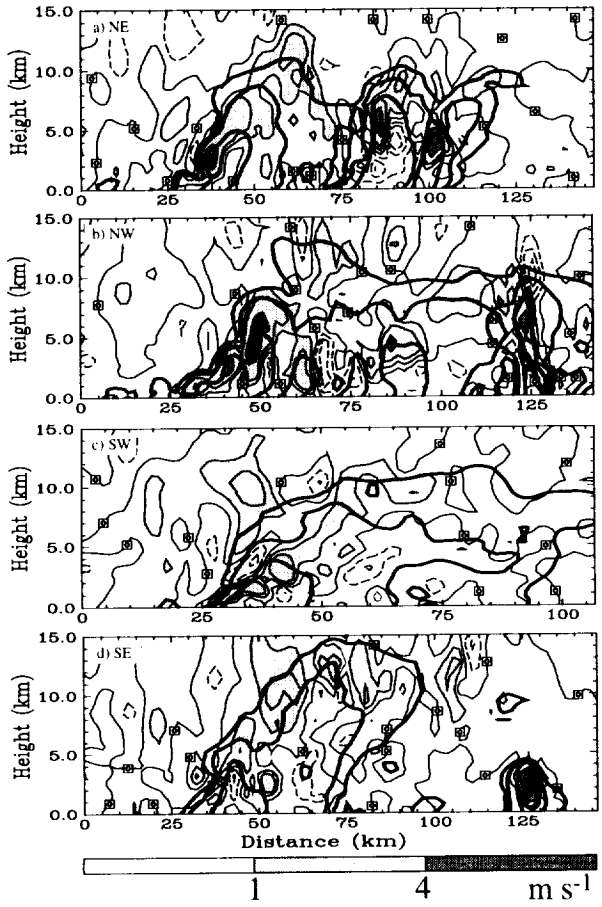

Figure 11. Vertical velocity (thin contours and shading) and radar reflectivity (bold contours) for radial cross sections starting at storm center and extending to the (a) northeast, (b) northwest, (c) southwest, and (d) southeast of the storm. Cross section locations are indicated in Fig. 7c. Vertical velocity contours are drawn at 0 and +/– 1, 2, 4, 6, and 8 m s^{-1}. Reflectivity contours are drawn at 15, 30, and 45 dBZ.

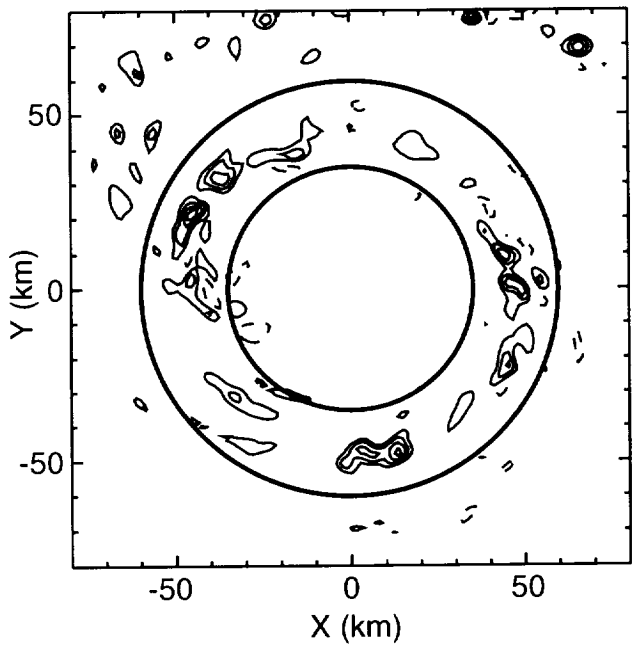

Figure 13. Horizontal distribution of vertical velocity at 5.2 km MSL and 66 h. The contour interval is 2 m s^{-1} with the zero contour excluded. Rings at 35 and 60 km radius indicate the annular region used to compute statistics in the eyewall.

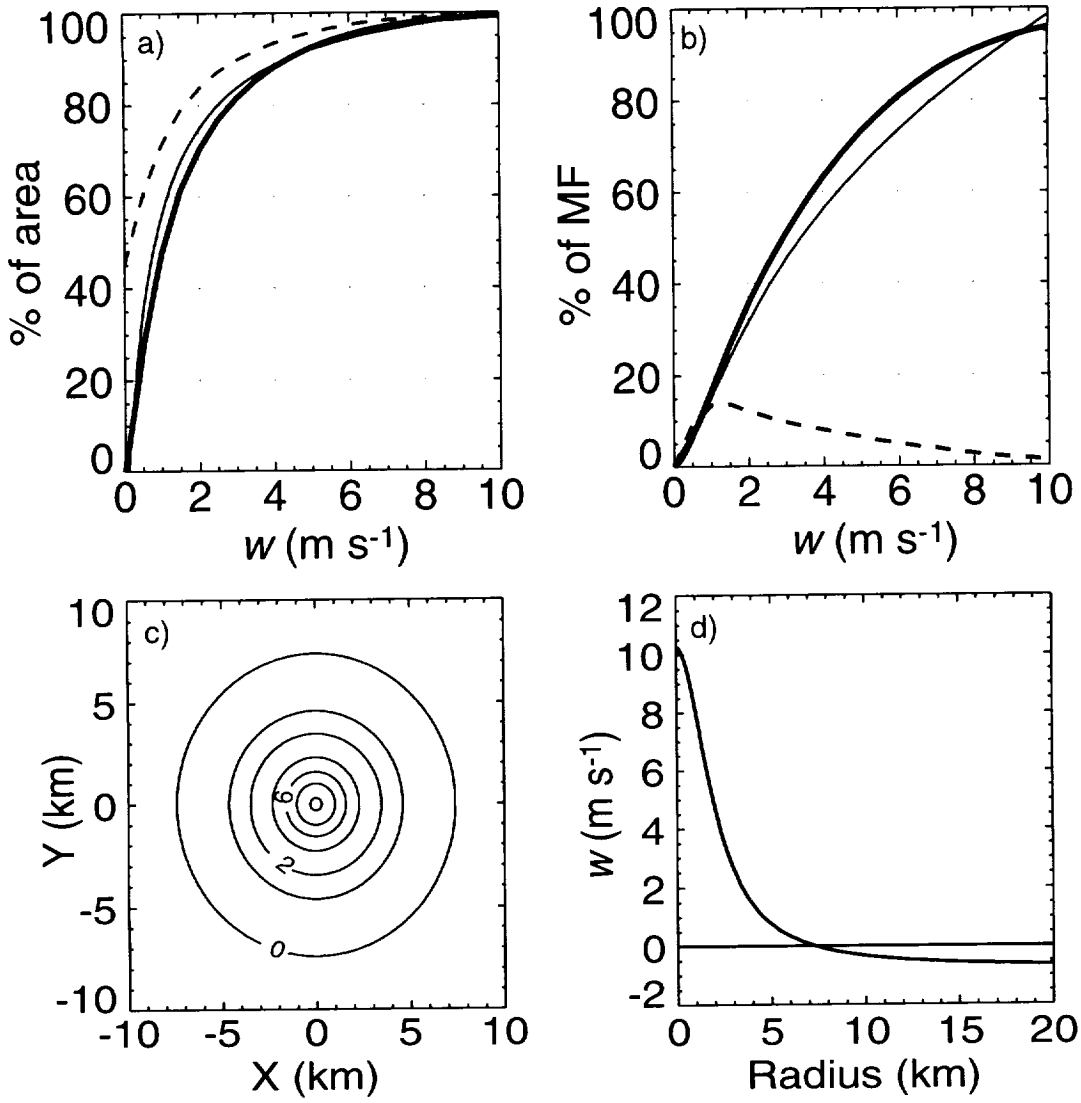

Figure 14. (a) Curves show the cumulative percentage of the area occupied by all updrafts less than the magnitude given on the abscissa. The dashed line shows the percentage of the total eyewall area while the thick solid line shows the percentage of the total updraft area in the eyewall (i.e., excludes the areas occupied by downdrafts). The thin solid line is similar to the thicker line, but corresponds to the hypothetical updraft in panels (c) and (d). (b) The dashed line shows the percentage of the upward mass flux associated with updrafts falling within 0.5 m s^{-1} bins centered on the indicated values of vertical velocity. The thick solid line indicates the cumulative percentage of the upward mass flux coming from updrafts less than the indicated value. The thin solid line corresponds to the hypothetical updraft. (c) The horizontal distribution of vertical velocity associated with a hypothetical circular updraft core. Contours are drawn at 2 m s^{-1} intervals with an additional contour at 1 m s^{-1}. (d) The radial distribution of vertical velocity associated with the hypothetical updraft, where the radius refers to the distance from the updraft center.

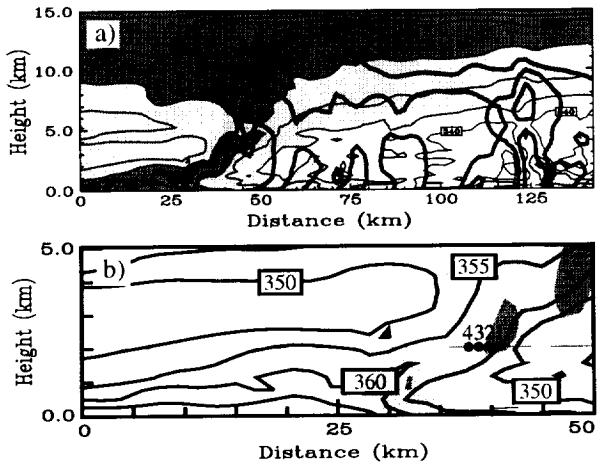

Figure 15. (a) Vertical cross section of θ_e (thin lines, shading) and radar reflectivity (bold contours) for the northwest cross section (cf. Fig. 7c). The contour interval for θ_e is 5 K, with light (dark) shading indicating values greater than 345 K (355 K). Reflectivity contours are drawn at 15, 30, and 45 dBZ. (b) θ_e (contours) and vertical velocity (shading) for a subset of the region in (a). Light (dark) shading corresponds to vertical velocities greater than 1 m s^{-1} (4 m s^{-1}). Trajectory locations are indicated by the dots with the numbers 1-4 identifying the trajectories.

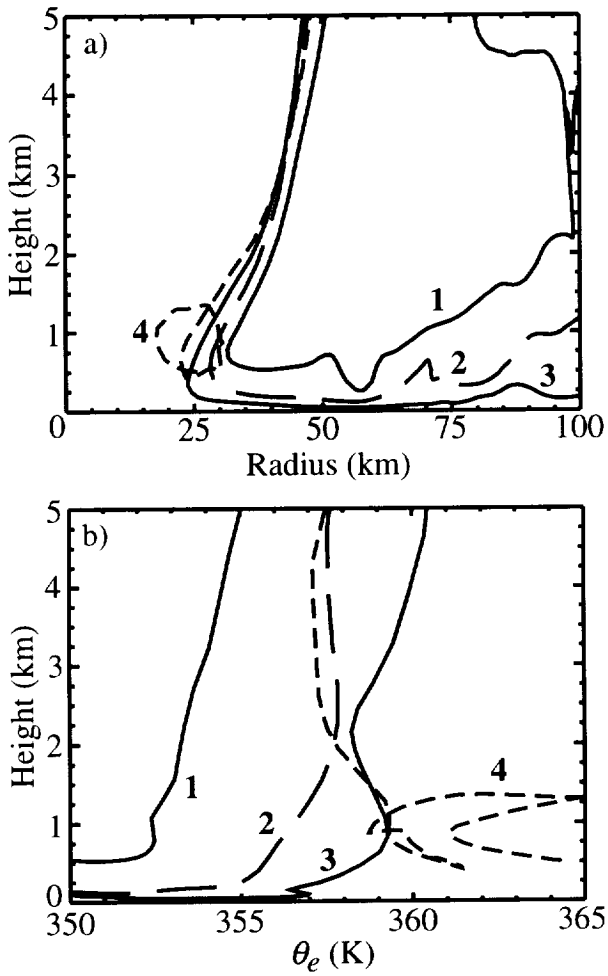

Figure 16. (a) Profiles of trajectory radius versus height for the trajectories with initial positions indicated in Fig. 15b. Only radii less than 100 km are shown. (b) Trajectory θ_e versus height. Only θ_e values greater than 350 K are shown.

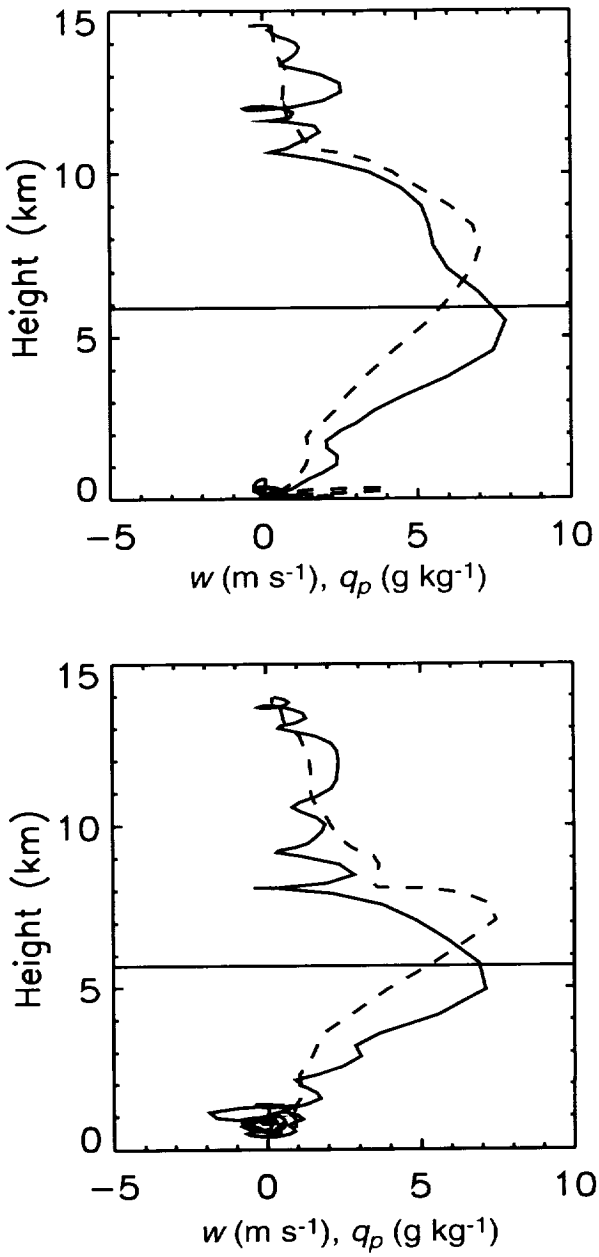

Figure 17. Profiles of vertical velocity (solid line) and total hydrometeor mixing ratio (q_p, dashed line) versus height for (a) trajectory 3 and (b) trajectory 4.

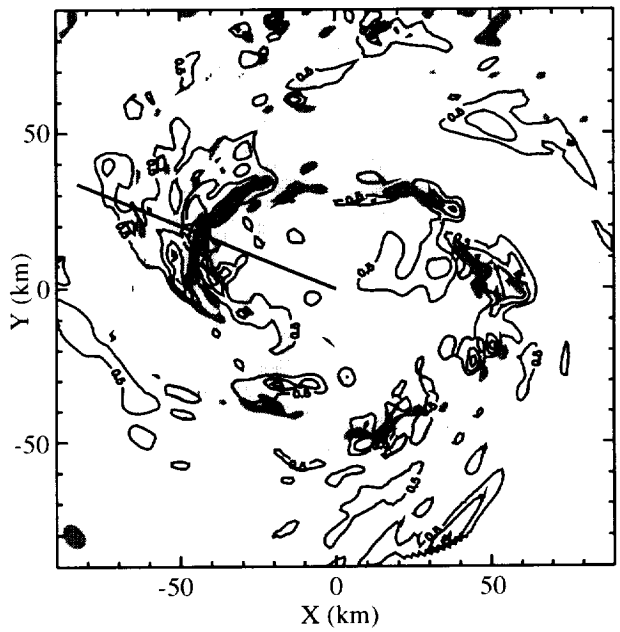

Figure 18. Horizontal cross section at 3.2 km MSL and 66 h of vertical velocity (light shading > 1 m s^{-1}, dark shading > 3 m s^{-1}) and perturbation virtual potential temperature (positive contours only, drawn at 1 K intervals starting at 0.5 K) associated with wavenumbers 2 and higher. The line indicates the location of the vertical cross sections in Fig. 19.

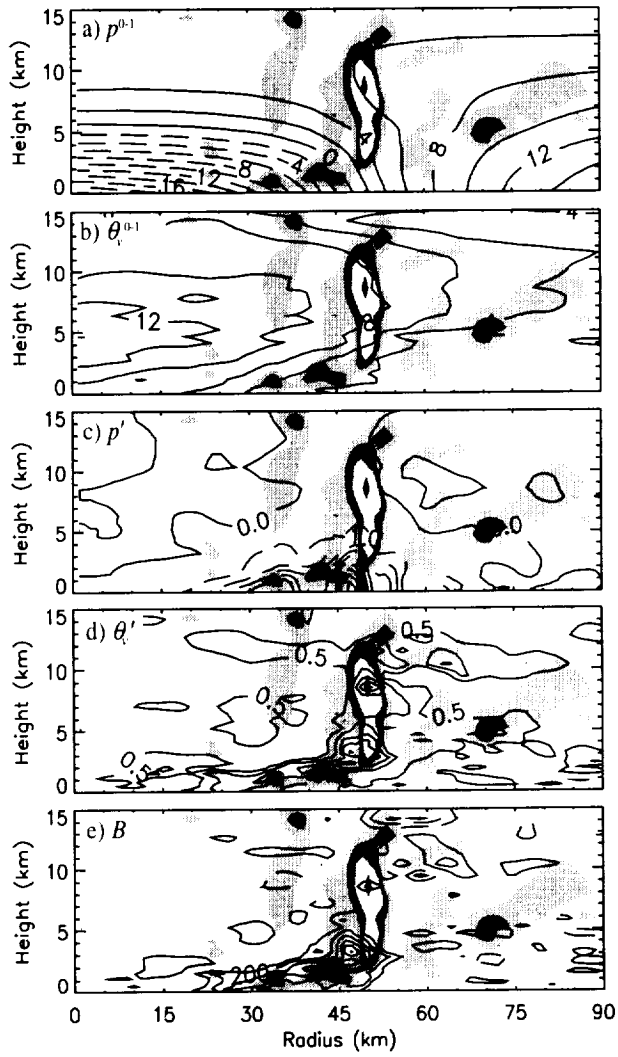

Figure 19. Vertical cross sections of (a) $p^{0,1}$ (2 hPa contour interval), (b) $\theta_v^{0,1}$(2 K interval), (c) p (wavenumbers 2 and higher, 0.5 hPa interval), (d) θ_v (1 K intervals starting at 0.5 K), and (e) buoyancy B (100 m s^{-1} h^{-1} intervals starting at 100 m s^{-1} h^{-1}). In (d, e), only positive values are contoured for clarity.

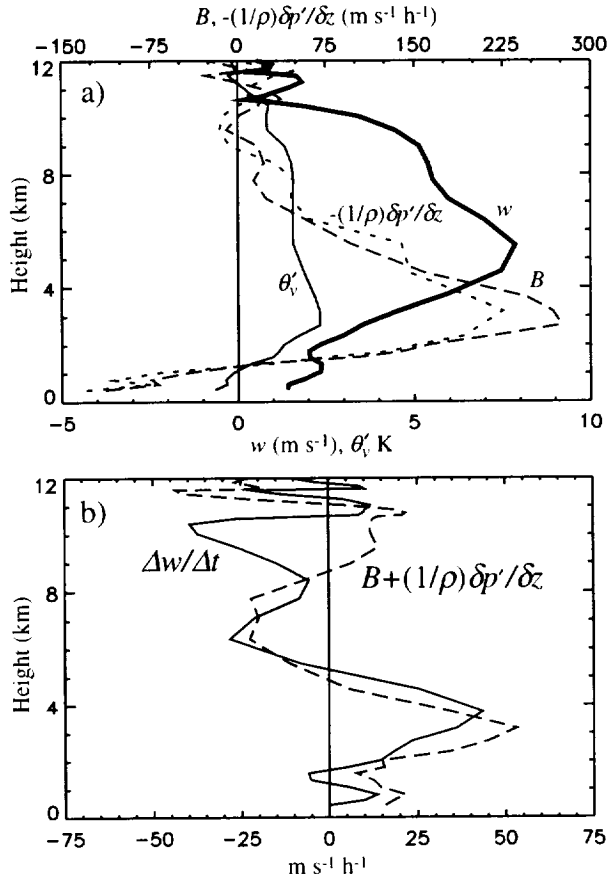

Figure 20. (a) Vertical profiles of w (thick solid line), θ_v' (thin solid line), B (dashed line), and the vertical perturbation pressure gradient force (dotted line) following trajectory 3. (b) Profiles of the vertical velocity tendency (solid line) and the vertical force balance (dashed line).

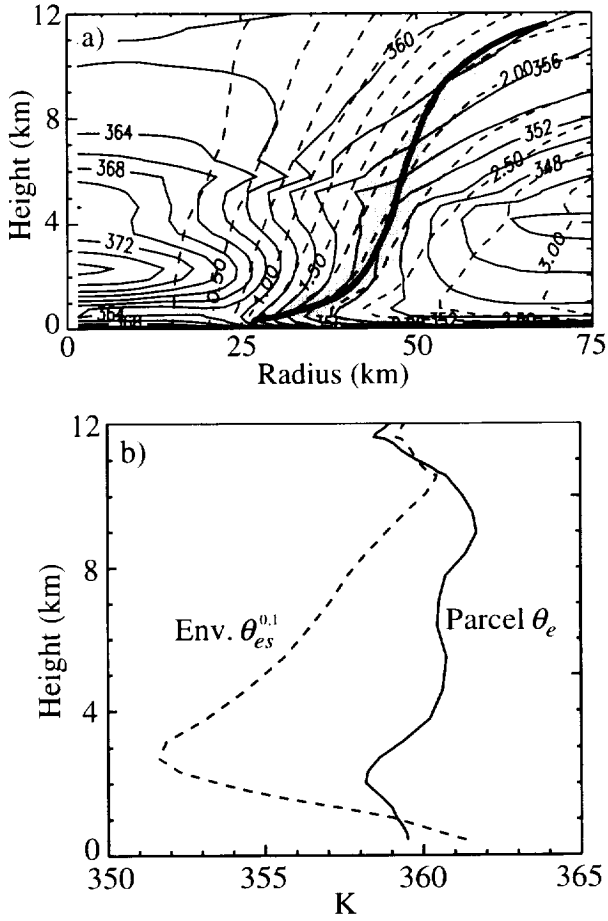

Figure 21. (a) Radial cross section of the azimuthal mean θ_{es} (solid lines, 2 K intervals) and M (dashed lines, 0.25×10^6 s^{-1} intervals). The light shading indicates the area of the azimuthal mean eyewall updraft while the thick solid line depicts a typical air parcel trajectory in the radius-height plane. (b) Profiles of environmental θ_{es} (dashed line) and air parcel θ_e (solid line) following an air parcel rising in the eyewall [obtained from trajectory 3, but intended here to illustrate profiles along the bold line in (a)].

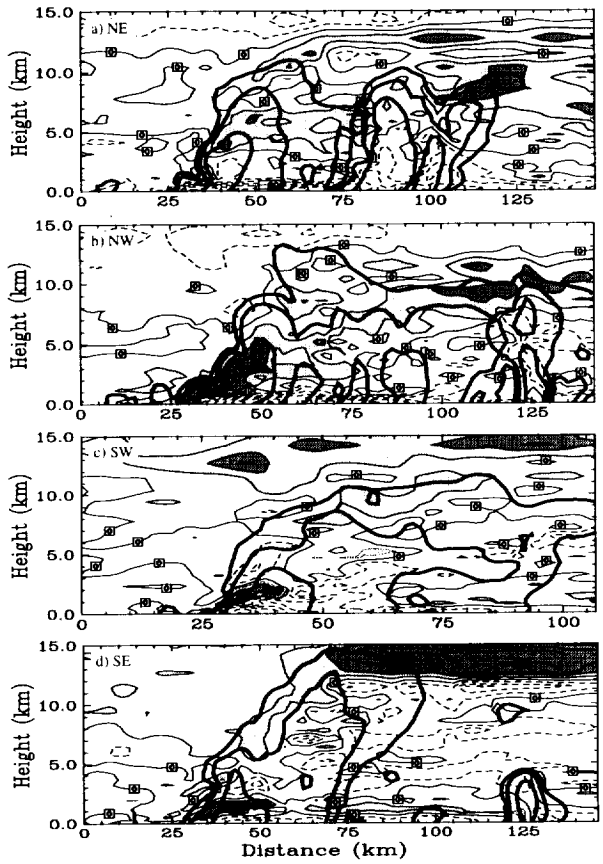

Figure 12. As in Fig. 11, but for radial velocity, contour interval of 5 m s^{-1}, with light (dark) shading indicating outflow greater than 5 m s^{-1} (10 m s^{-1}).

A cloud-resolving simulation of Hurricane Bob (1991): Storm structure and eyewall buoyancy

Scott A. Braun

Summary

A computer simulation of a hurricane is conducted using a model with a horizontal grid spacing that is capable of resolving individual clouds. The model produces a realistic hurricane that intensifies slowly during the period of simulation. When averaged over time, the results reveal the effects of storm motion and vertical and horizontal variations in the environmental wind on the structure of inflow into the storm, rising motion in the wall of thunderstorms that surrounds the eye (known as the eyewall), and the associated precipitation. Instantaneous model fields show that inflow into the eyewall is very intense and shallow and transitions to strong outward flow just above the bases of the clouds in the eyewall. Statistical calculations indicate that the most of the upward motion in the hurricane eyewall is associated with a small number of intense but isolated thunderstorm updrafts instead of a broader region of more gentle upward motion, consistent with the concept of hot cloud towers.

Tongues of warm, moist air are seen along the inner edge of the eyewall updraft and within the low-level outward flow. This air originates primarily from outside of the eyewall and comes from the layer closest to the surface after penetrating closest to the storm center. The eye of the hurricane contains very warm air at upper levels that is generally believed to reduce or prevent the release of instabilities that produce thunderstorms. Some hypotheses suggest that the instability, rather than being released in the vertical direction, is instead released only along a slanted path outward and upward. This study shows that the low-level outward flow displaces the rising air sufficiently far away from the warm air in the eye so that the instability can be released in the vertical direction to produce thunderstorms rather than requiring that the air rise along a slanted path.